Supplementary Information

Modulating solvation structure to enhance amorphous solid electrolyte interface formation for ultra-stable aqueous zinc anode

Guifang Zeng,‡[abc] Qing Sun,‡*[abc] Sharona Horta,[d] Paulina R. Martínez-Alanis,[c] Peng Wu,[ab] Jing Li,[ac] Shang Wang,[ab] Maria Ibáñez,[d] Yanhong Tian,*[ab] Lijie Ci,*[a] and Andreu Cabot*[ce]

[a] *State Key Laboratory of Precision Welding & Joining of Materials and Structures, Harbin Institute of Technology, Harbin 150001, China*

[b] *Zhengzhou Research Institute, Harbin Institute of Technology, Zhengzhou 450000, China*

[c] *Catalonia Institute for Energy Research – IREC, Sant Adrià de Besòs, Barcelona 08930, Spain*

[d] *IST Austria, Am Campus 1, Klosterneuburg 3400, Austria*

[e] *ICREA Pg. Lluis Companys, Barcelona 08010, Spain*

‡ *These authors contributed to this work equally.*

Experimental Section

Materials

Zn foils (99.99%) and Cu foils (99.99%) were purchased from Guangdong Canrd New Energy Technology. $ZnSO_4$, $Zn(CF_3COO)_2$, and V_2O_5 were purchased from Sigma-Aldrich. The preparation of the electrolyte uses high-purity water.

Preparation of Electrolytes

The electrolytes were prepared by dissolving $ZnSO_4 \cdot 7H_2O$ and $Zn(CF_3COO)_2$ into deionized water. First, we prepared 2 M $ZnSO_4$ as the base electrolyte (ZS). Then we added 10, 50, 80, and 100 mM $Zn(CF_3COO)_2$. The obtained electrolytes were denoted as ZSF-10, ZSF-50, ZSF-80 (ZSF), and ZSF-100, respectively.

Characterizations

Scanning electron microscopy (SEM) was performed on an Auriga Zeiss field emission. Bruker AXS D8 X-ray diffraction (XRD) was used to analyze the crystalline structures. TEM characterization was performed on a JEOL JEM2800 microscope. For the cryo-TEM and cryo-HRTEM characterizations, the Cu grid was transferred into a cryo-TEM equipped low-dose system. TOF-SIMS characterizations were conducted on an ION TOF ToF-SIMS 5-100. A Renishaw Invia Reflex Raman was used for Raman spectra. Bruker FTIR was employed to determine the vibrational peaks. The X-ray photoelectron spectroscopy (XPS) was obtained with ESCALAB 250 (Al Kα). The pH values are tested by a GLP 22 meter.

Simulation methods

First-principles calculations were performed using the DMol3 module. The generalized gradient approximation (GGA) and Becke–Lee–Yang–Parr (BLYP) functionals were employed to describe electron interaction energies. Ultrasoft pseudopotential was performed (OTFG describing the valence electrons) with Grimme's method introduced for DFT-D correction. The self-consistent field (SCF) tolerance was set to 5×10^{-7} eV $atom^{-1}$, with a cutoff energy of 500 eV and a maximum of 500 cycles. Additionally, a vacuum space of 20 Å was included in each model. the adsorption energy (ΔE) was acquired by the following equation: $\Delta E = E_{total} - E_{atom} - E_{mol}$ (E_{total}, the total energy of the system; E_{atom}, the total energy of matrix; and E_{mol}, total energy of Zn^{2+}). In terms of the diffusion energy barrier calculations, transition state (TS) search tasks were implemented using the DMol3 module. Geometry optimizations were conducted prior to the TS search simulations. MD simulations were conducted using the Forcite module. The forcefield was set to be COMPASSIII and the electrostatic employed Ewald electrostatic method with the van der Waals method assigned as atom based. The forcefield types were assigned according to the states of the atoms. Geometry optimizations were conducted prior to the MD simulations. To enhance the efficiency of the MD simulations, parallel calculations were performed. Both first-principles and MD simulations were exerted based on Materials Studio platform. The finite element analyses of Zn plating were conducted using ANYSES based on Nernst–Planck–Poisson equation. In terms of the electrochemistry on the Zn anode surface, the concentration-dependent Butler–Volmer equation was introduced. Semiellipse nuclei were set at the initial state at the Zn anode surface.

Electrochemical Measurements

The 2032-type coin cells were used for all the electrochemical testing in this work. For the $Zn||V_2O_5$ full cell, the positive electrode was prepared with 70 wt% V_2O_5 as active material, 20 wt% black carbon as conductive agent, and 10 wt% PVDF as binder. All the galvanostatic discharge/charge tests were measured on a Neware battery testing system (Shenzhen, China) at room temperature. The cyclic voltammetry (CV), corrosion, linear sweep voltammetry (LSV) and linear polarization tests were obtained on a Correst electrochemical workstation.

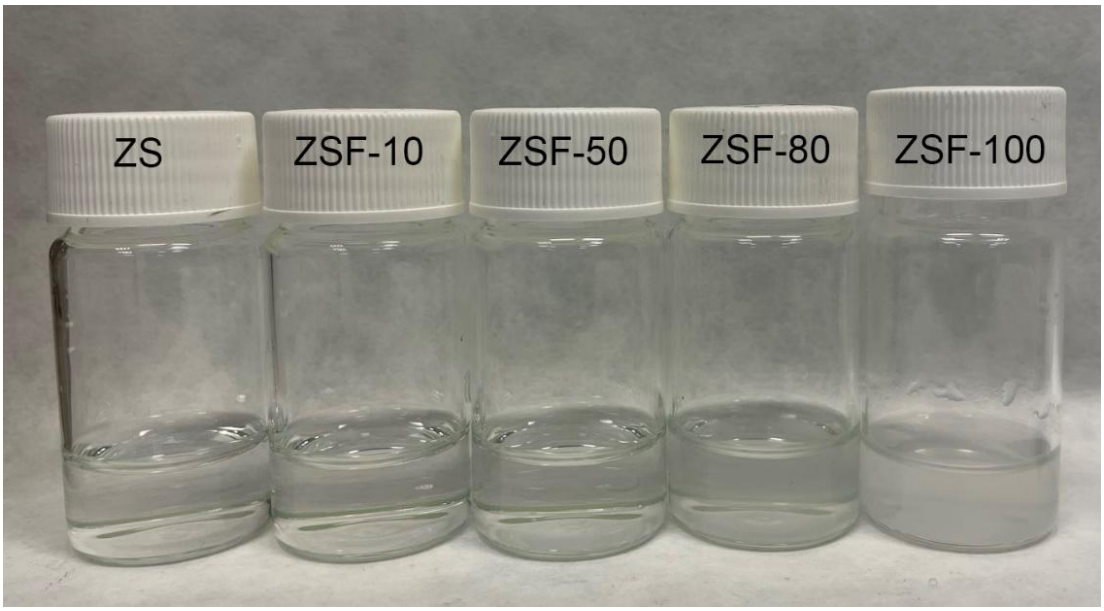

Fig. S1 The optical Fig.s of the electrolytes with different mount of additives.

As shown in the above photo, the solution becomes saturated when the additive concentration exceeds 80 mM. Therefore, we selected 10, 50, and 80 mM as the experimental groups.

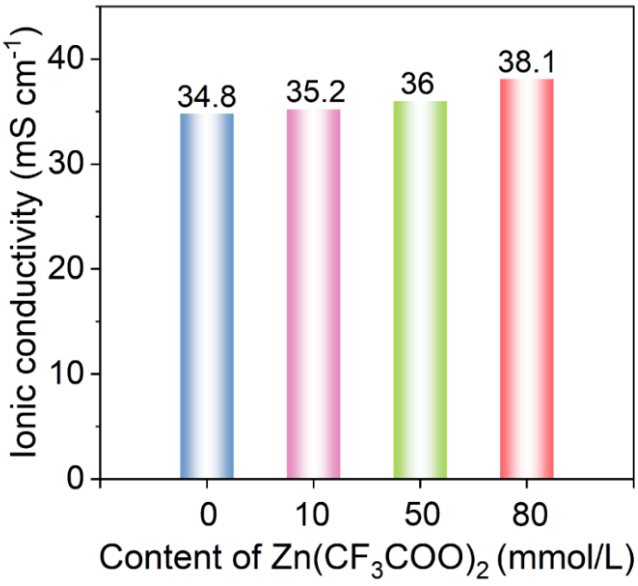

Fig. S2 The ionic conductivity of the electrolytes with different amounts of additives.

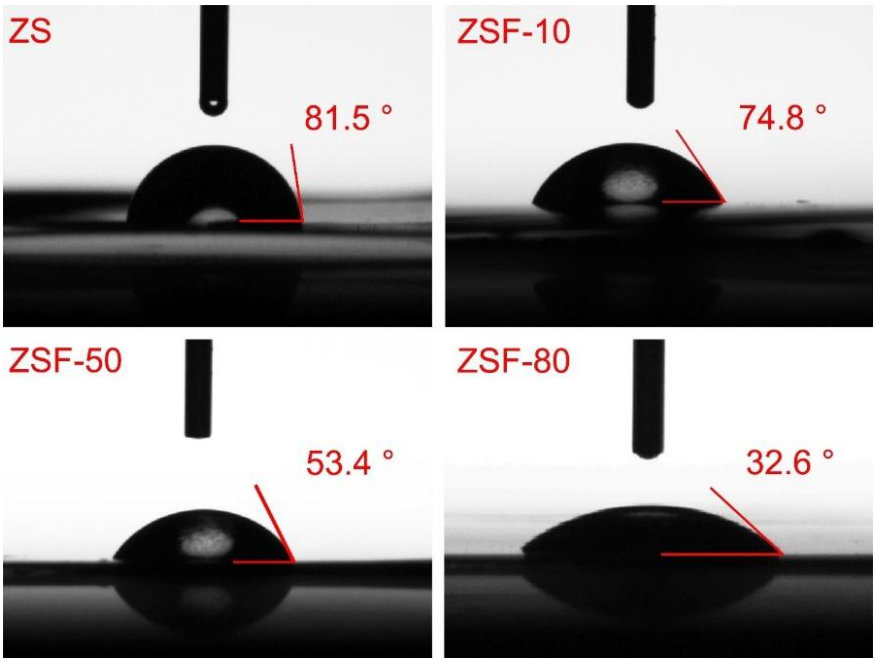

Fig. S3 The contact angles of electrolytes (with different amounts of additives) on the Zn foils.

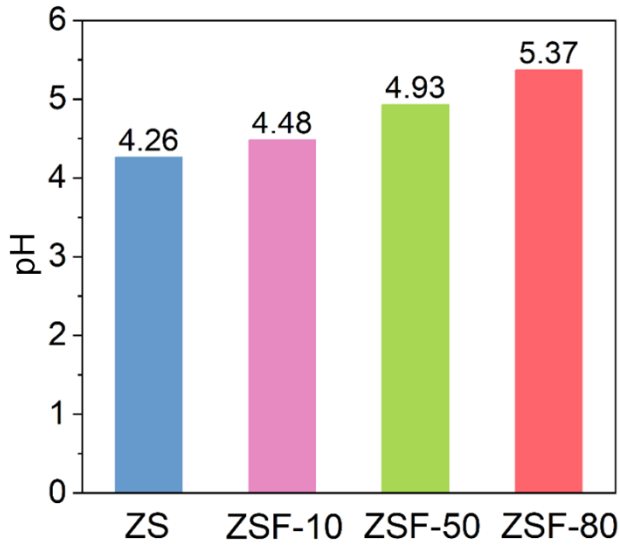

Fig. S4 The pH values with different amounts of additives.

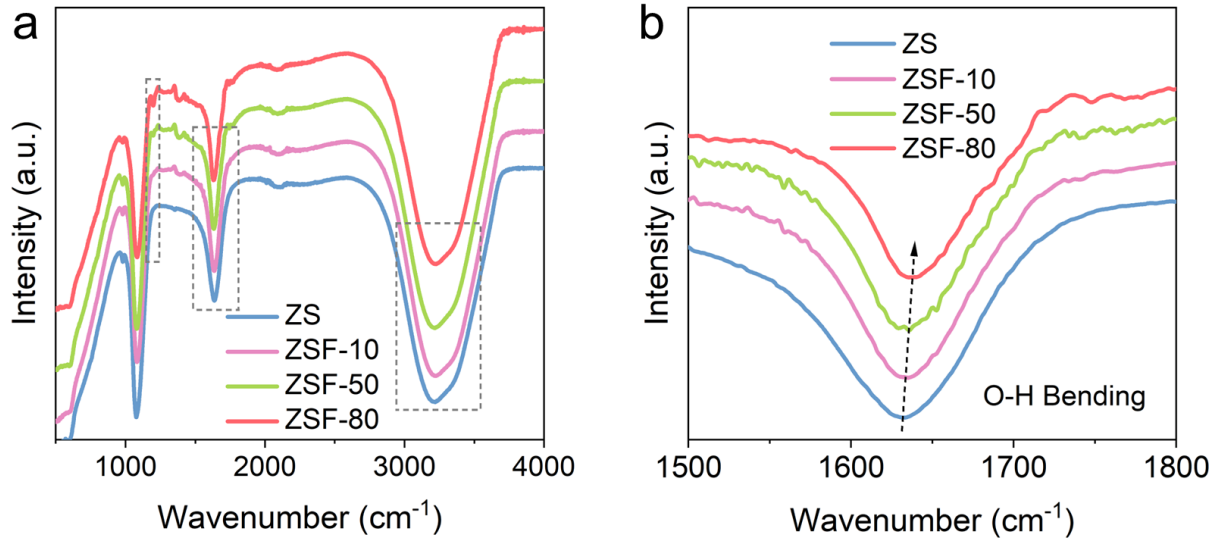

Fig. S5 (a, b) The FTIR patterns of different electrolytes.

Table S1 Structures of elementary units for theoretical simulations.

Elementary Unit	Ball and stick mode	Stick mode
Zn^0/Zn^{2+}		
H_2O		
SO_4^{2-}		
CF_3COO^-		

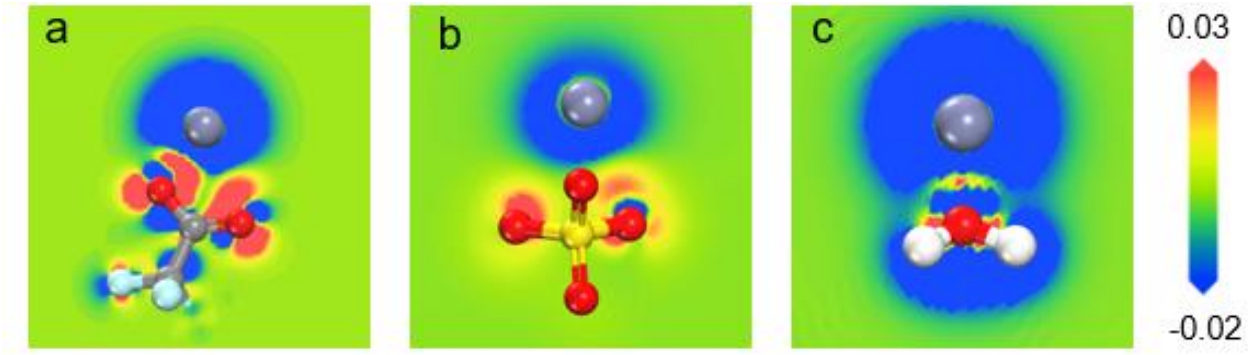

Fig. S6 (a-c) Theoretically calculated charge density differences of Zn^{2+}-TFA^- (a), Zn^{2+}-SO_4^{2-} (b), and Zn^{2+}-H_2O (c).

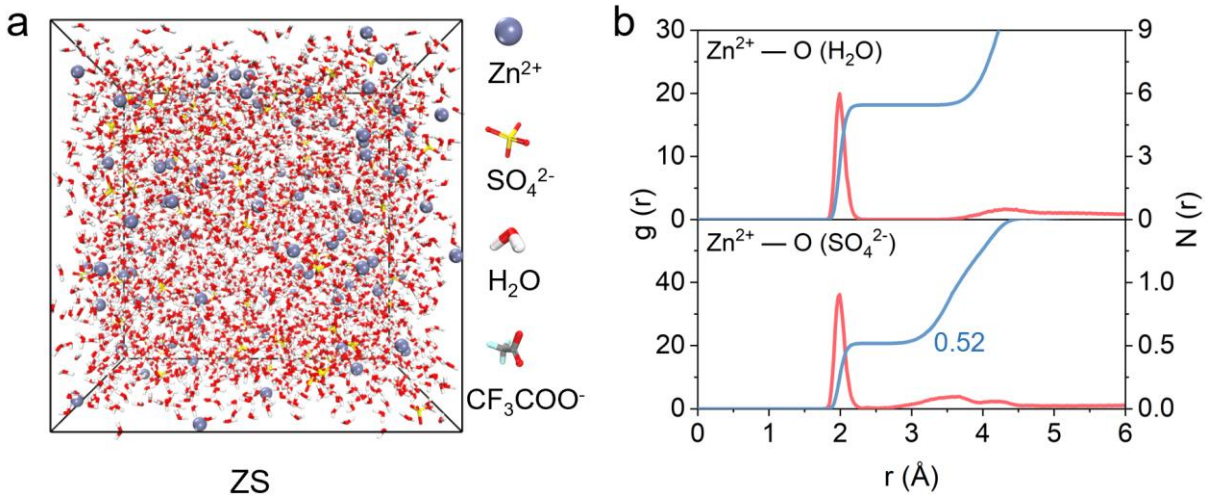

Fig. S7 (a) The 3D snapshot of ZS electrolyte from MD simulation. (b) RDF g (r) and corresponding integrated coordination numbers N (r) of Zn^{2+}-O (for H_2O) and Zn^{2+}-O (for SO_4^{2-}), respectively.

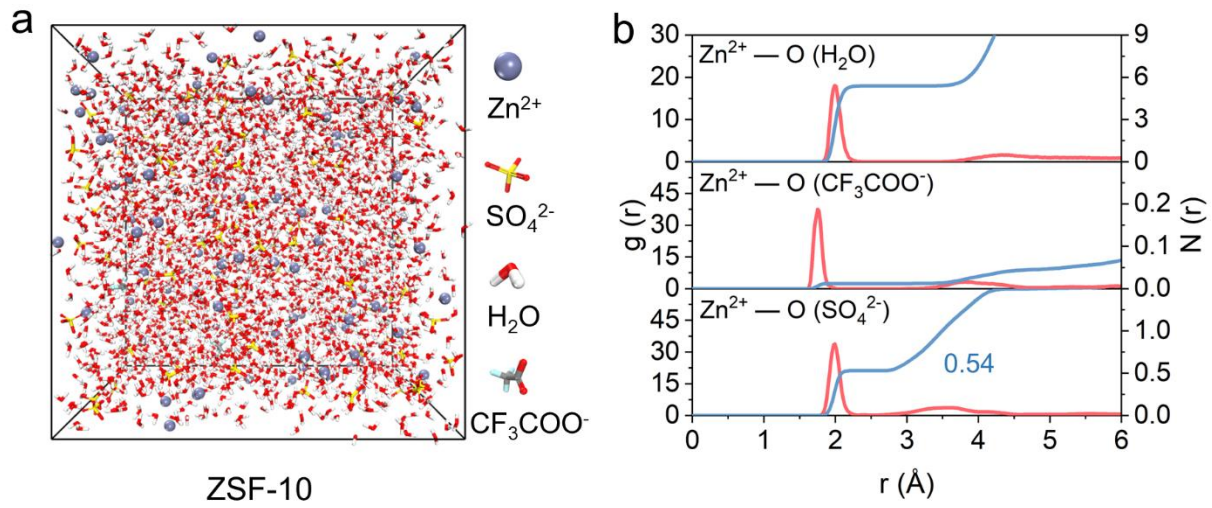

Fig. S8 (a) The 3D snapshot of ZSF-10 electrolyte from MD simulation. (b) RDF g (r) and corresponding integrated coordination numbers n (r) of Zn^{2+}-O (for H_2O), Zn^{2+}-O (for SO_4^{2-}), and Zn^{2+}-O (for CF_3COO^-), respectively.

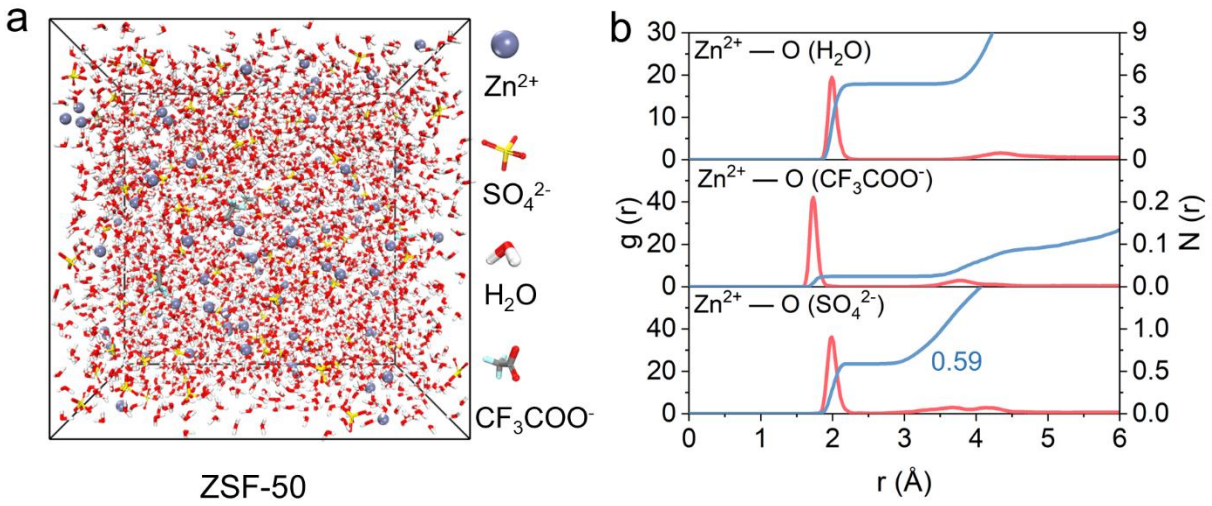

Fig. S9 (a) The 3D snapshot of ZSF-50 electrolyte from MD simulation. (b) RDF g (r) and corresponding integrated coordination numbers n (r) of Zn^{2+}-O (for H_2O), Zn^{2+}-O (for SO_4^{2-}), and Zn^{2+}-O (for CF_3COO^-), respectively.

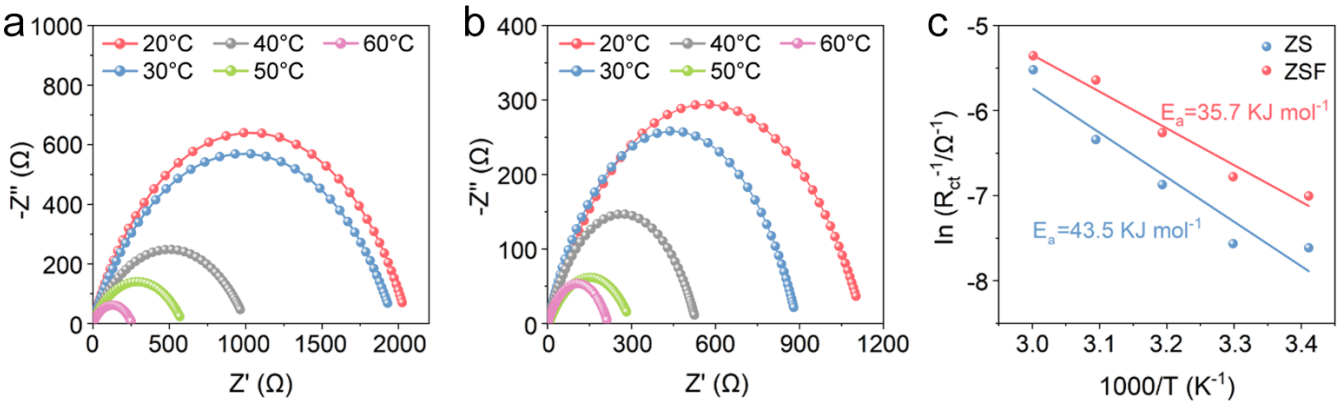

Fig. S10 EIS of the symmetrical Zn||Zn symmetric cells using (a) ZS and (b) ZSF electrolytes at different temperatures. (c) Arrhenius curves at different temperatures.

The desolvation process of Zn^{2+} ions are commonly regarded as the rate-limiting step in Zn deposition at the anode, and can be characterized by the activation energy (E_a) using the Arrhenius equation:

$$\frac{1}{R_{ct}} = A \exp\left(\frac{-E_a}{RT}\right)$$

Where R_{ct} represents the interface resistance, A is the frequency factor, R is the gas constant, and T stands for the absolute temperature.

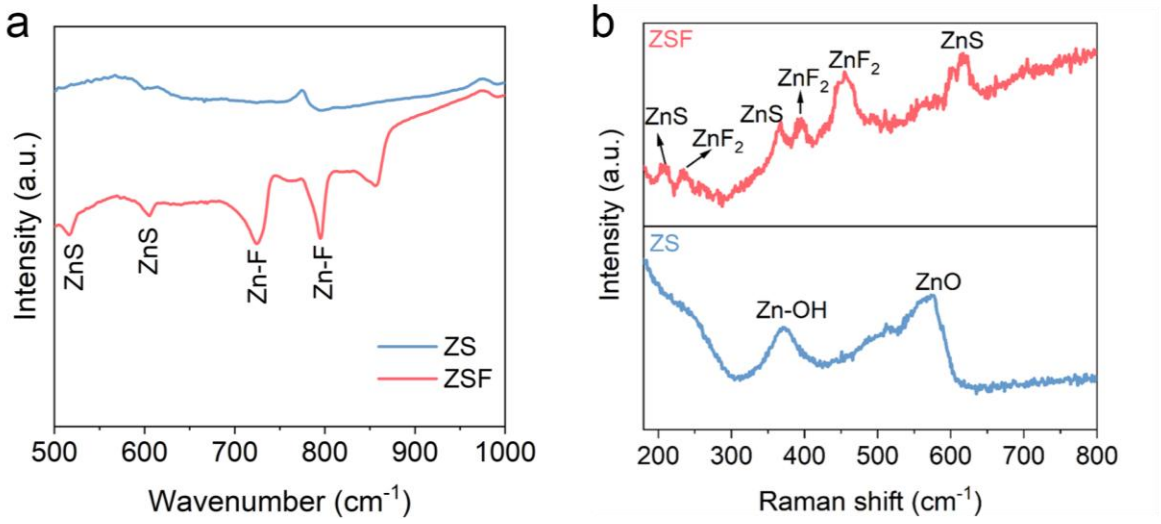

Fig. S11 (a, b) FTIR pattern (a) and Raman spectra (b) of the cycled Zn anodes after 100 cycles in ZS and ZSF electrolytes.

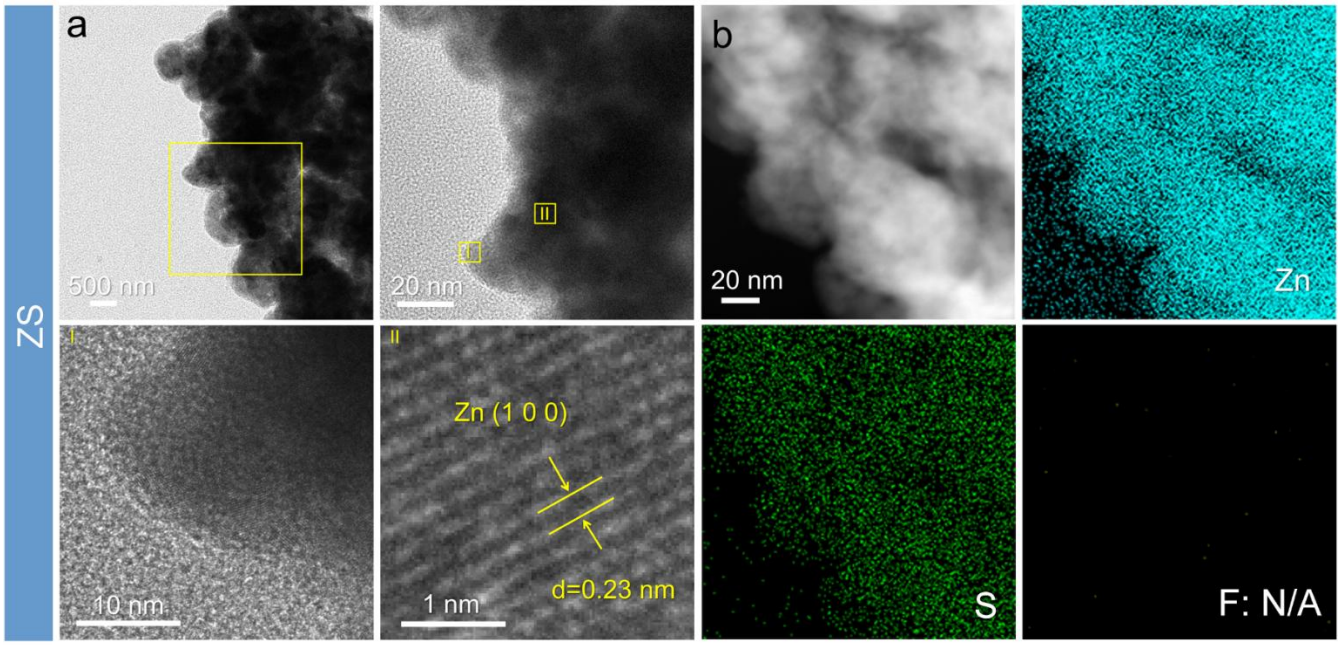

Fig. S12 (a, b) Cryo-TEM and HRTEM images (a) and corresponding EDX mapping of SEI (b) on the cycled Zn metal in ZS electrolyte.

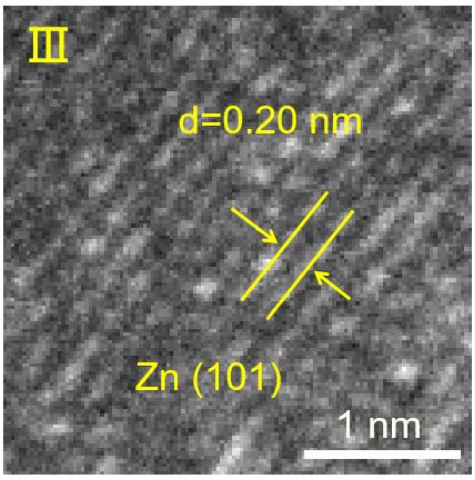

Fig. S13 The cryo-HRTEM of the Zn anode cycled in ZSF electrolyte.

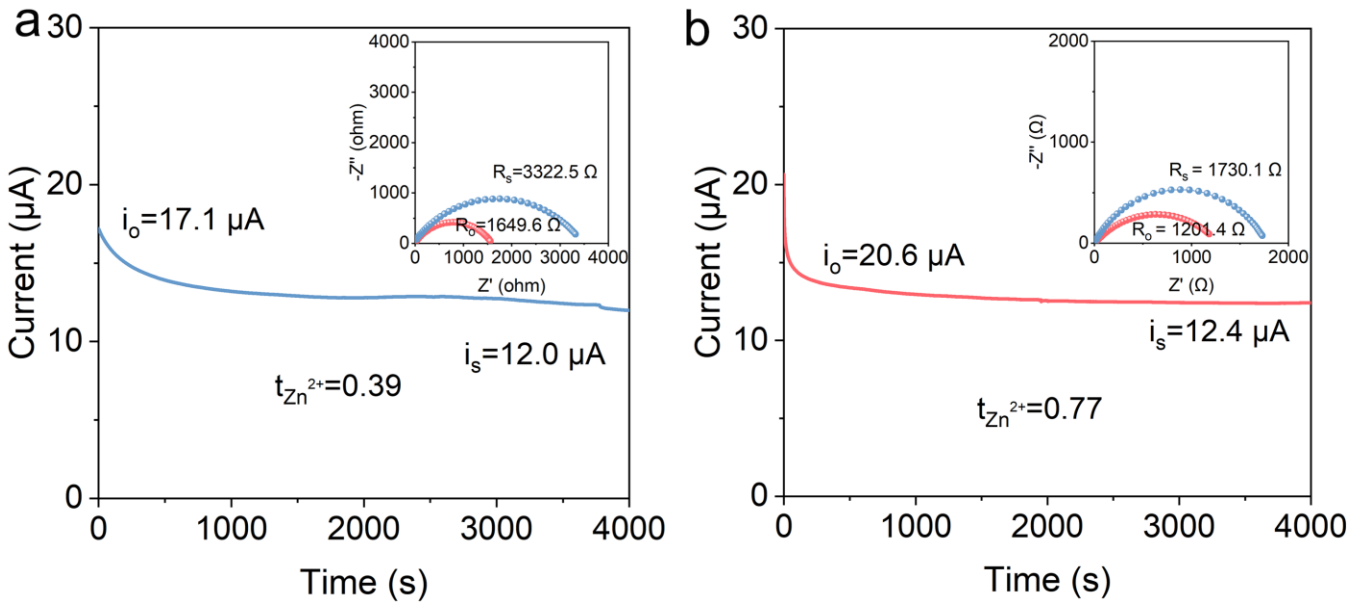

Fig. S14 Current-time plots of Zn||Zn symmetric cells in ZS (a) and ZSF (b) electrolyte after polarization at a constant potential (10 mV) for 4000s.

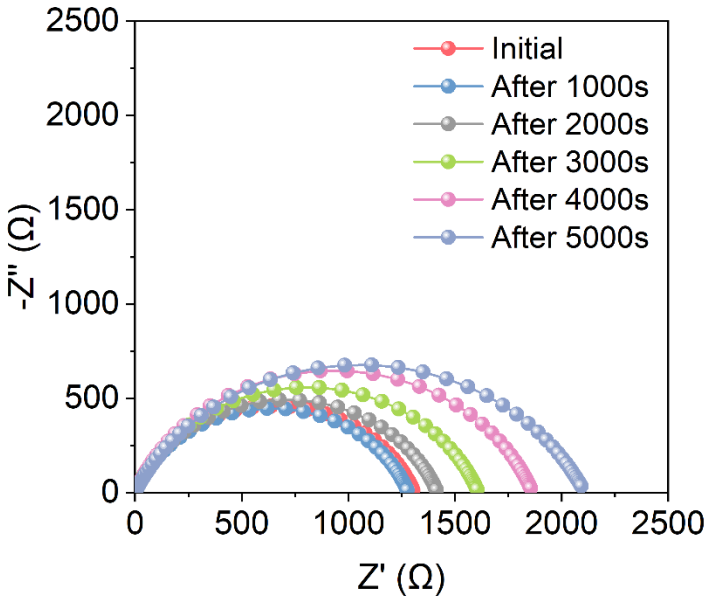

Fig. S15 EIS of Zn||Zn symmetric cells in ZSF electrolyte after polarization at a constant potential (10 mV) for different time.

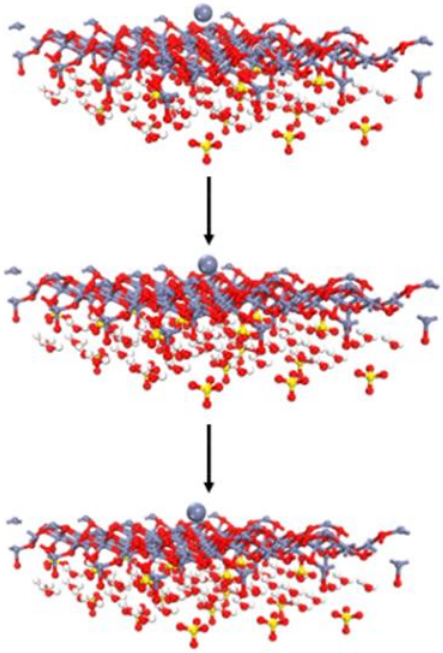

Fig. S16 The Diffusion paths and migration energy barriers of Zn^{2+} in ZSH.

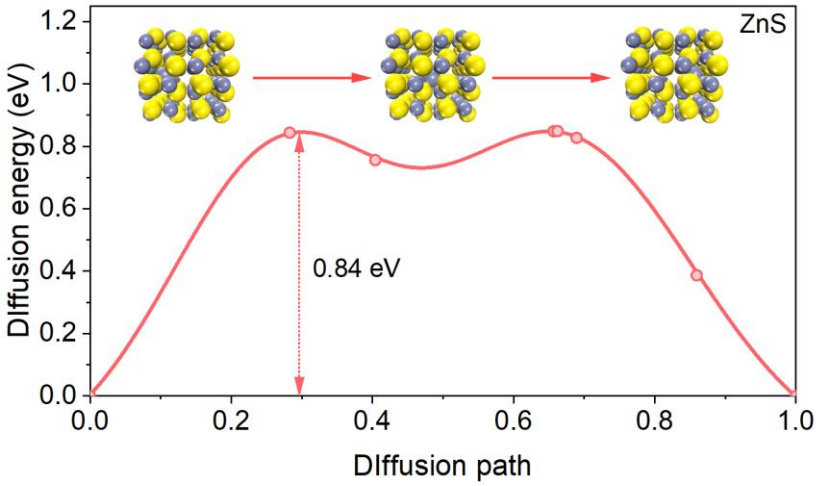

Fig. S17 Diffusion paths and migration energy barriers of Zn^{2+} in ZnS.

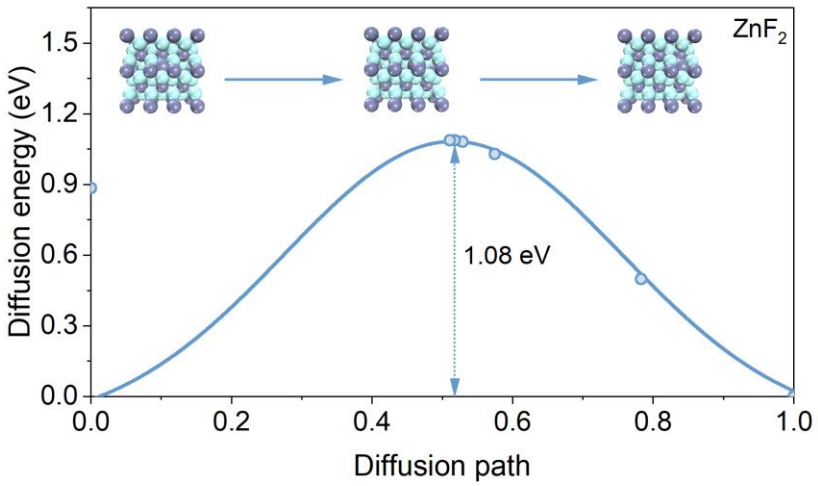

Fig. S18 Diffusion paths and migration energy barriers of Zn^{2+} in ZnF_2.

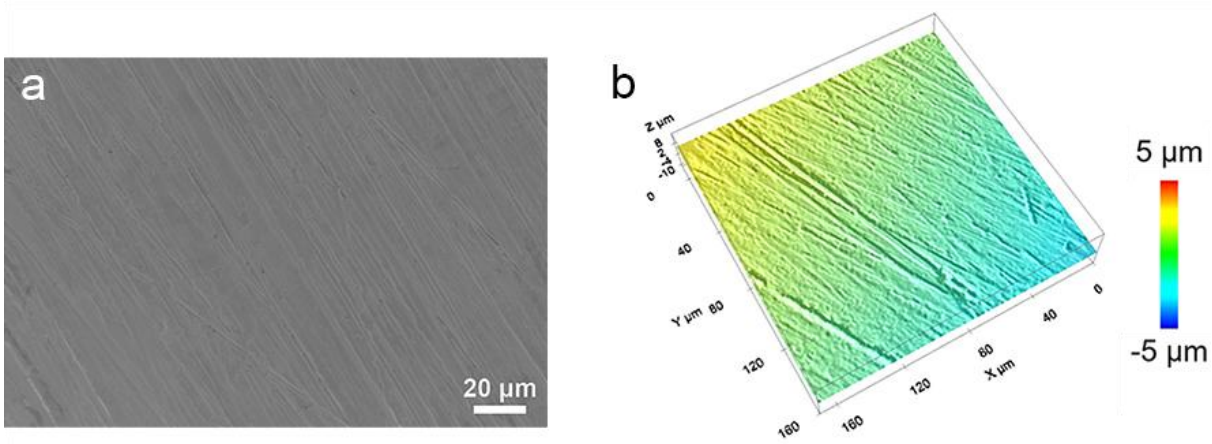

Fig. S19 (a, b) Morphology of pristine Zn anode. SEM (a) and 3D height (b) images.

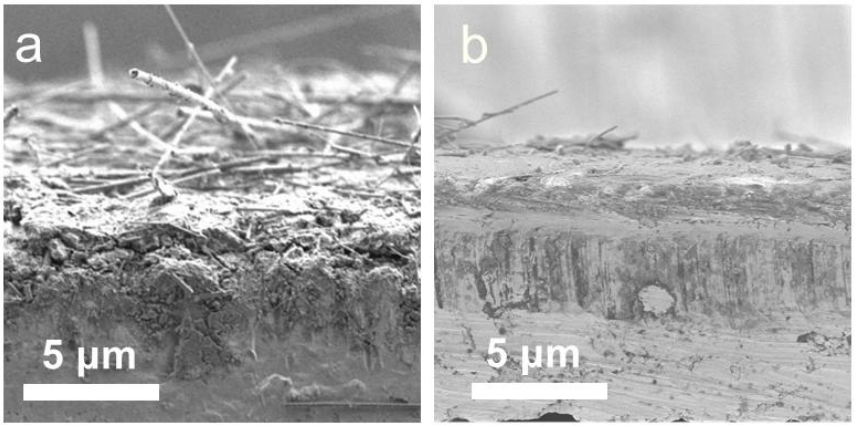

Fig. S20 (a, b) The section-cross SEM image of Zn anode after 1st plating in ZS (a) and ZSF (b) electrolytes.

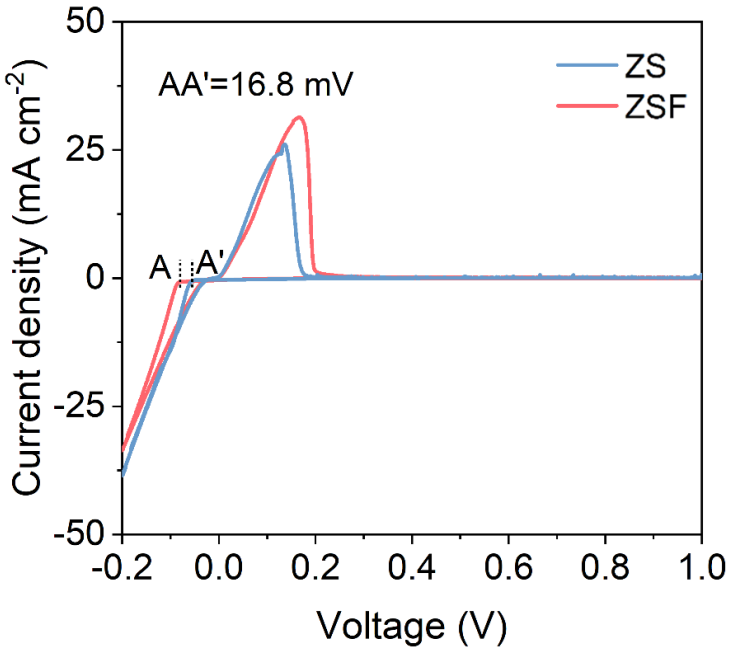

Fig. S21 The CV curves of the Zn||Cu cells at 1 mV S^{-1}.

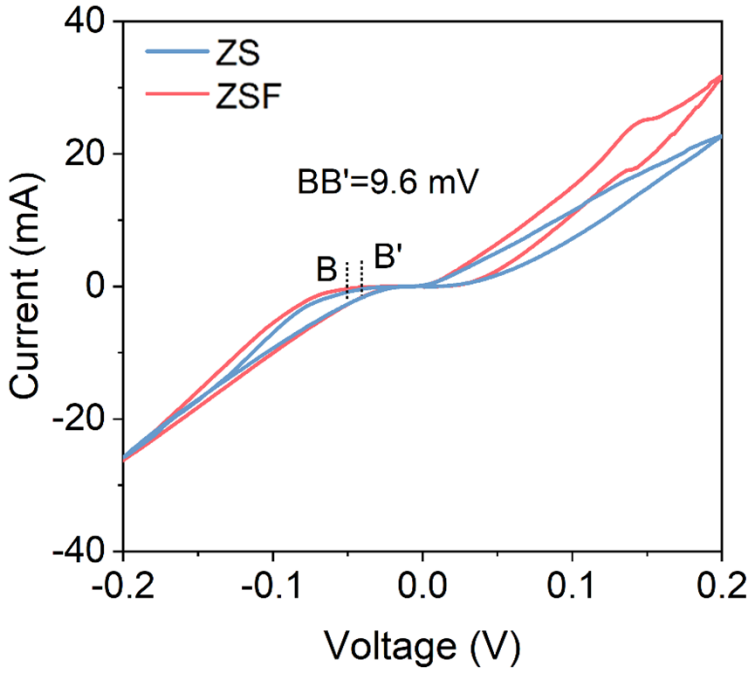

Fig. S22 The CV curves of the Zn||Zn cells at 1 mV S^{-1}.

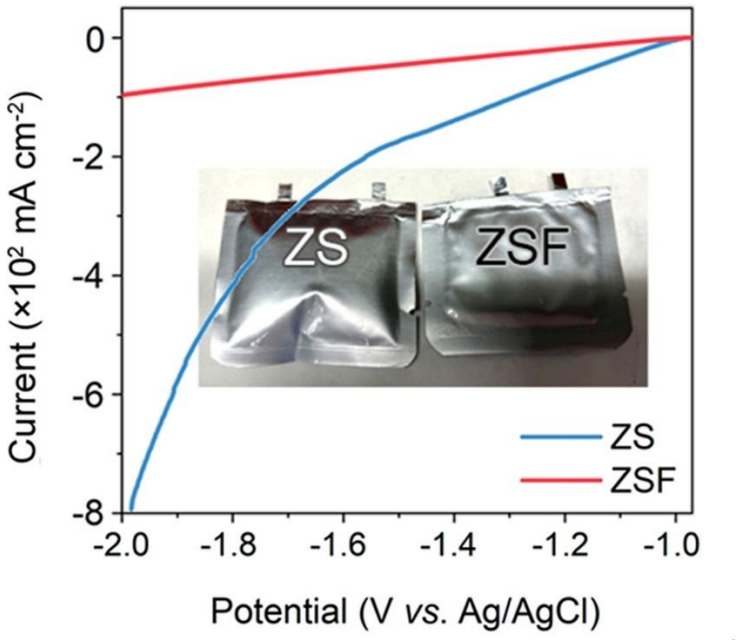

Fig. S23 LSV curves of ZS and ZSF electrolytes.

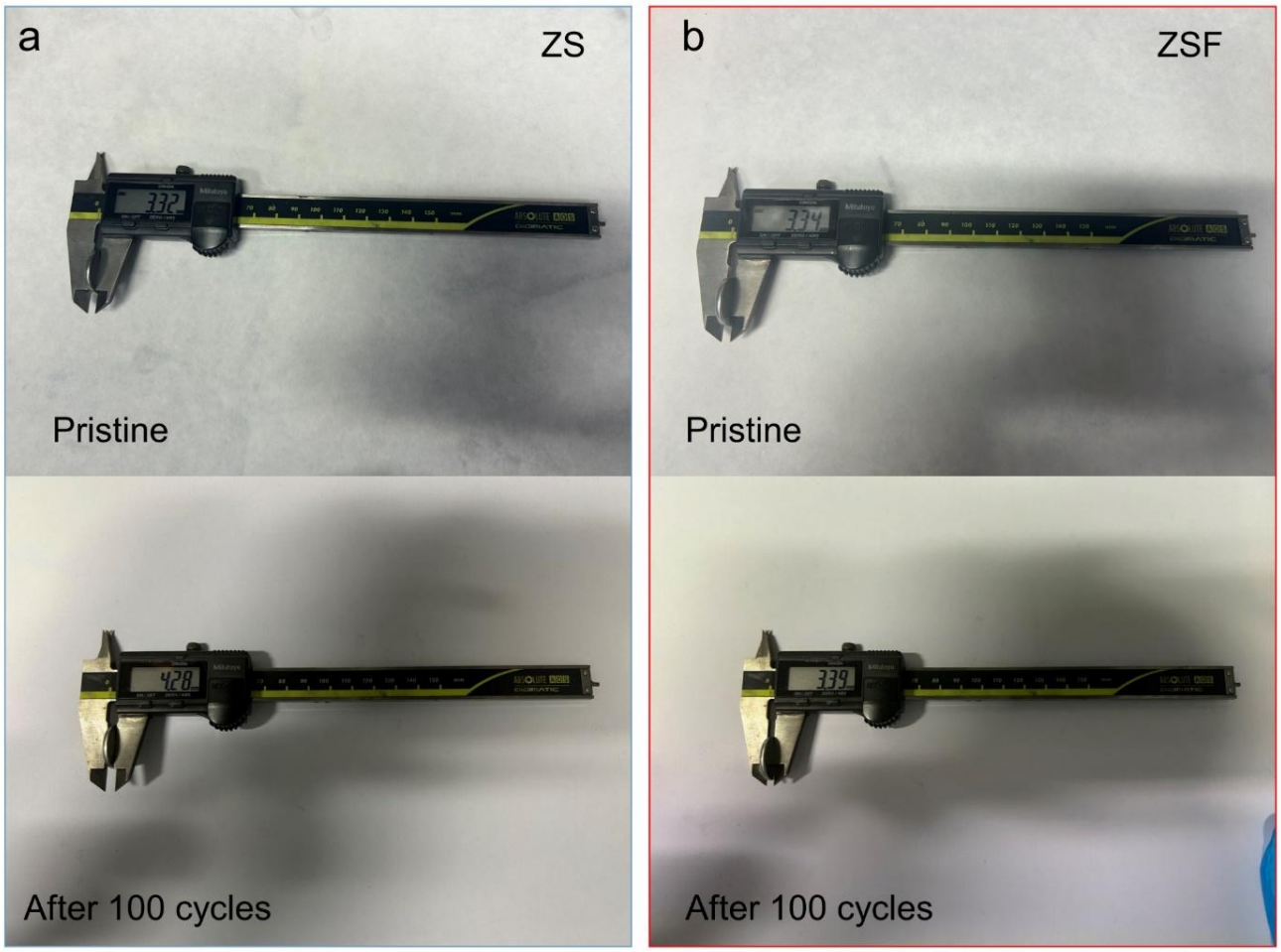

Fig. S24 The thickness variations of the cells using ZS (a) and ZSF (b) electrolytes after 100 cycles.

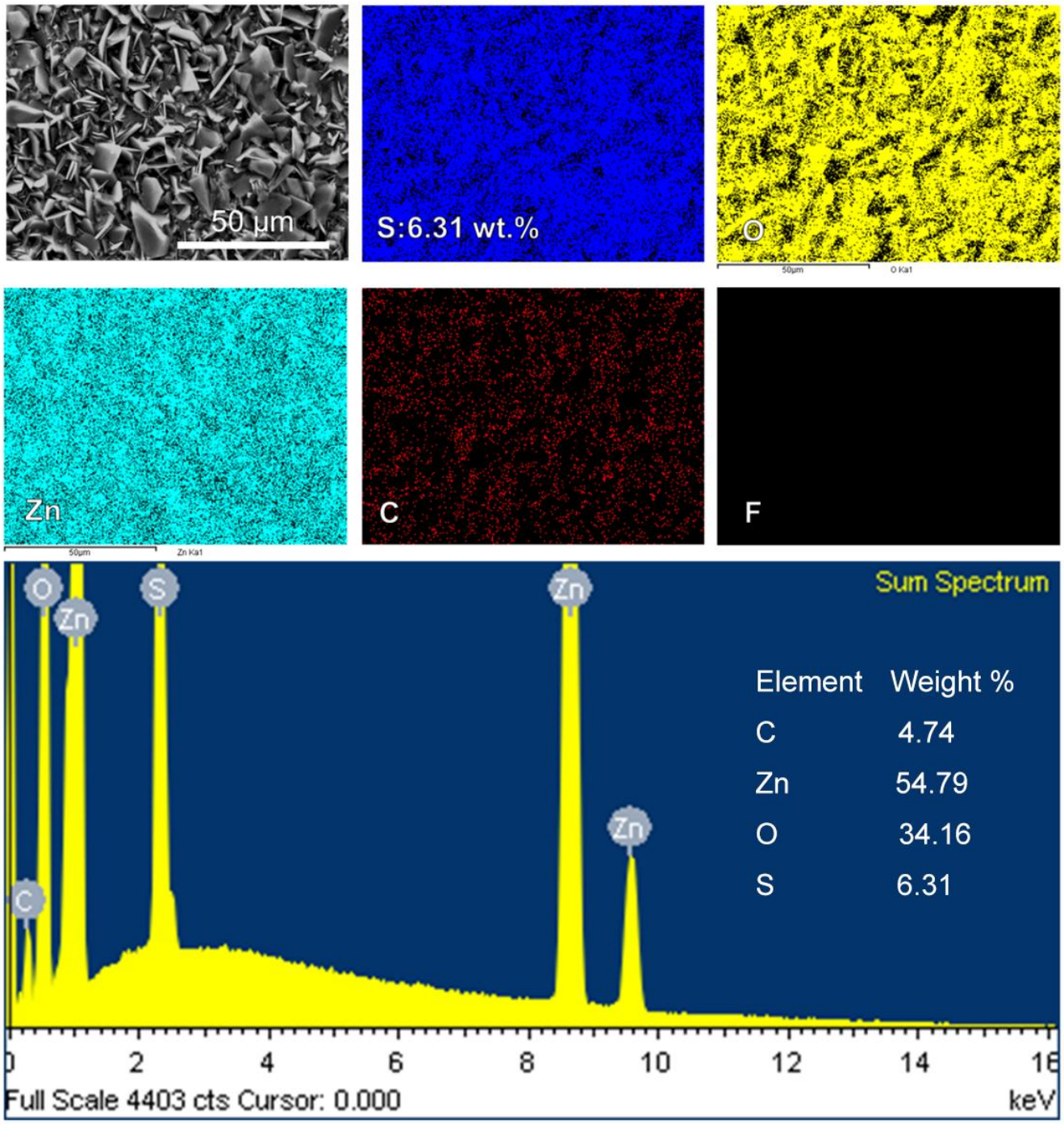

Fig. S25 The Zn anode soaked in the ZS electrolyte and the corresponding EDS mappings.

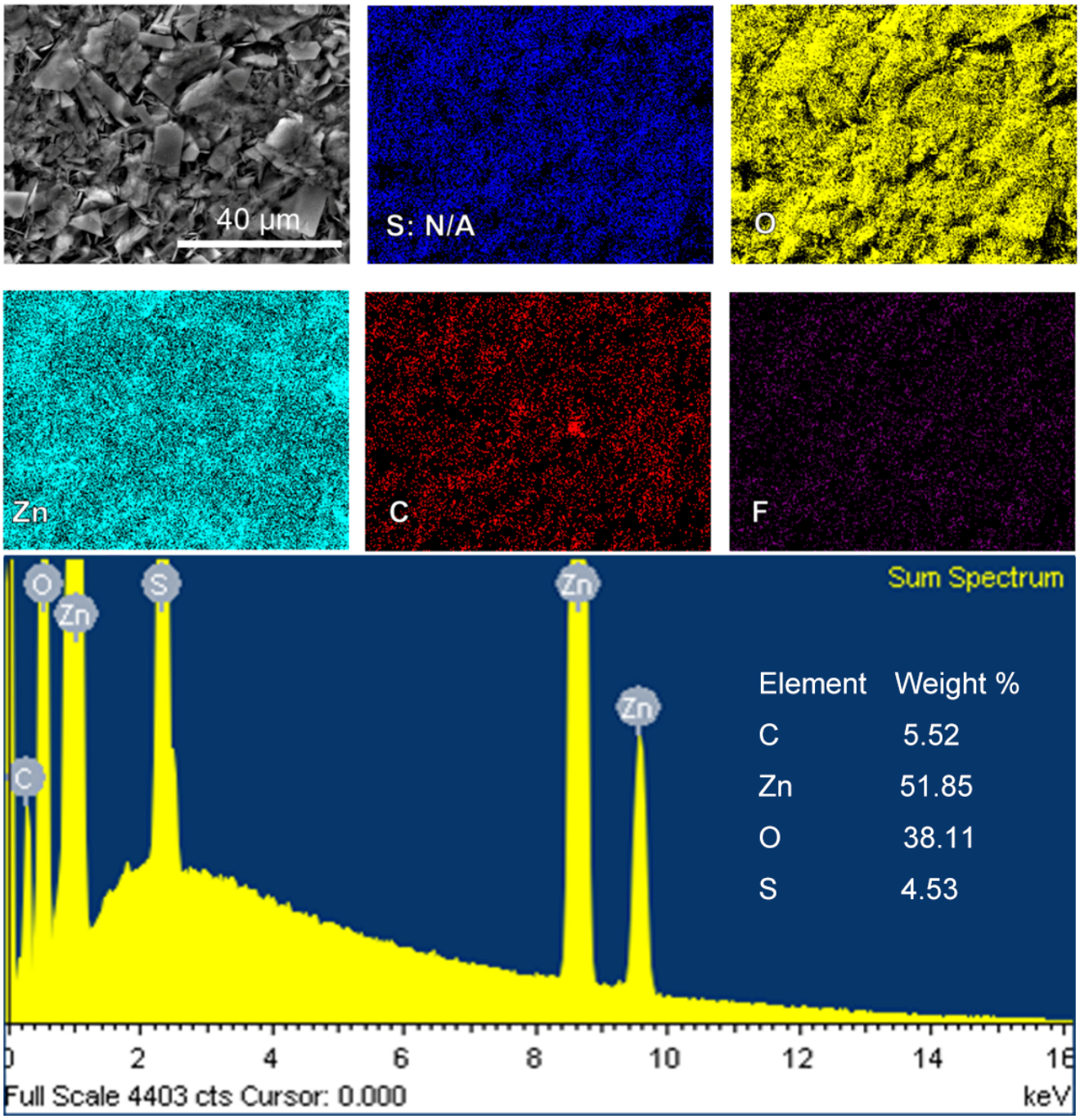

Fig. S26 The Zn anode and the corresponding EDS mappings soaked in the ZSF-10 electrolyte.

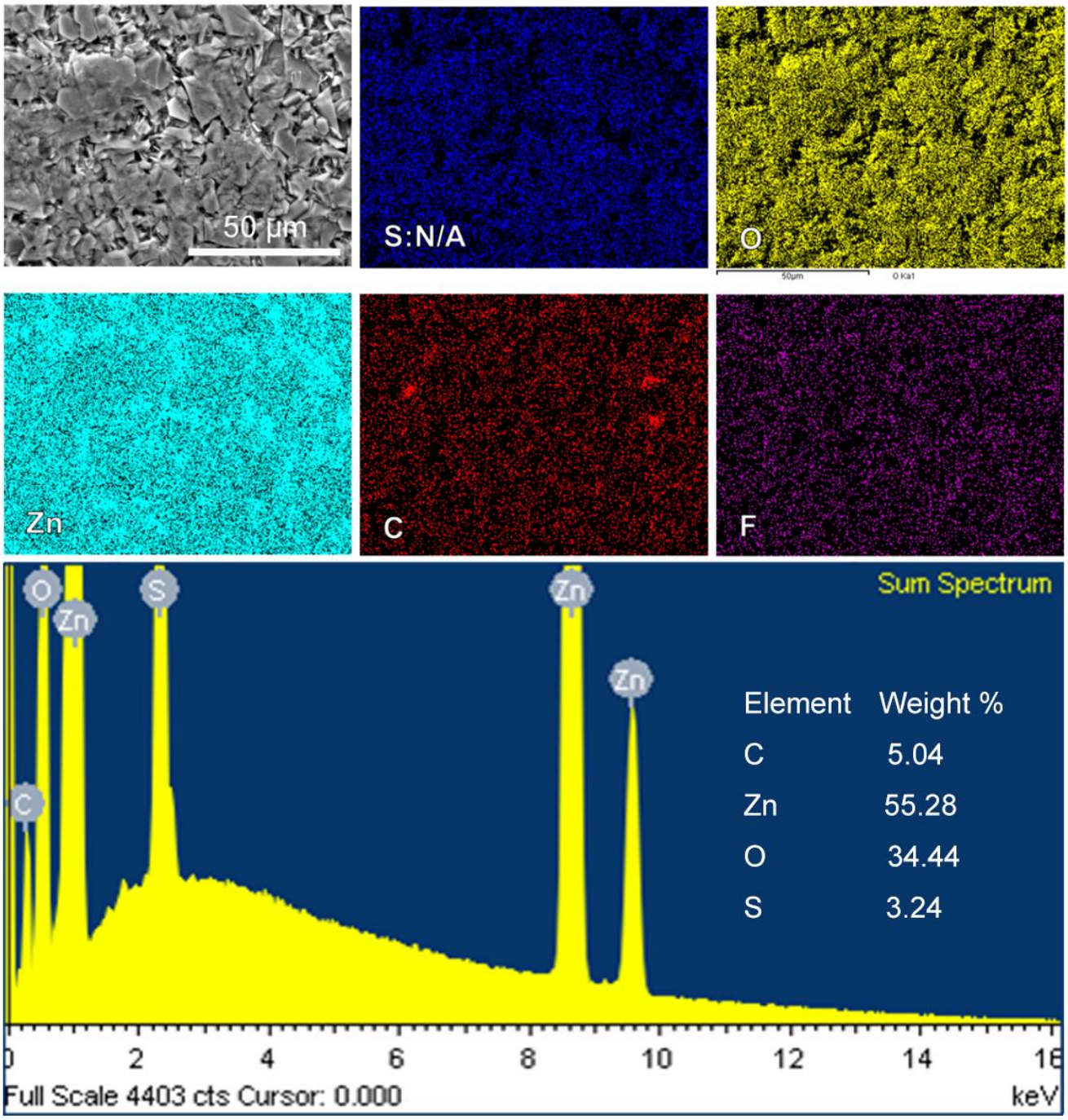

Fig. S27 The Zn anode and the corresponding S element EDS images soaked in the ZSF-50 electrolyte.

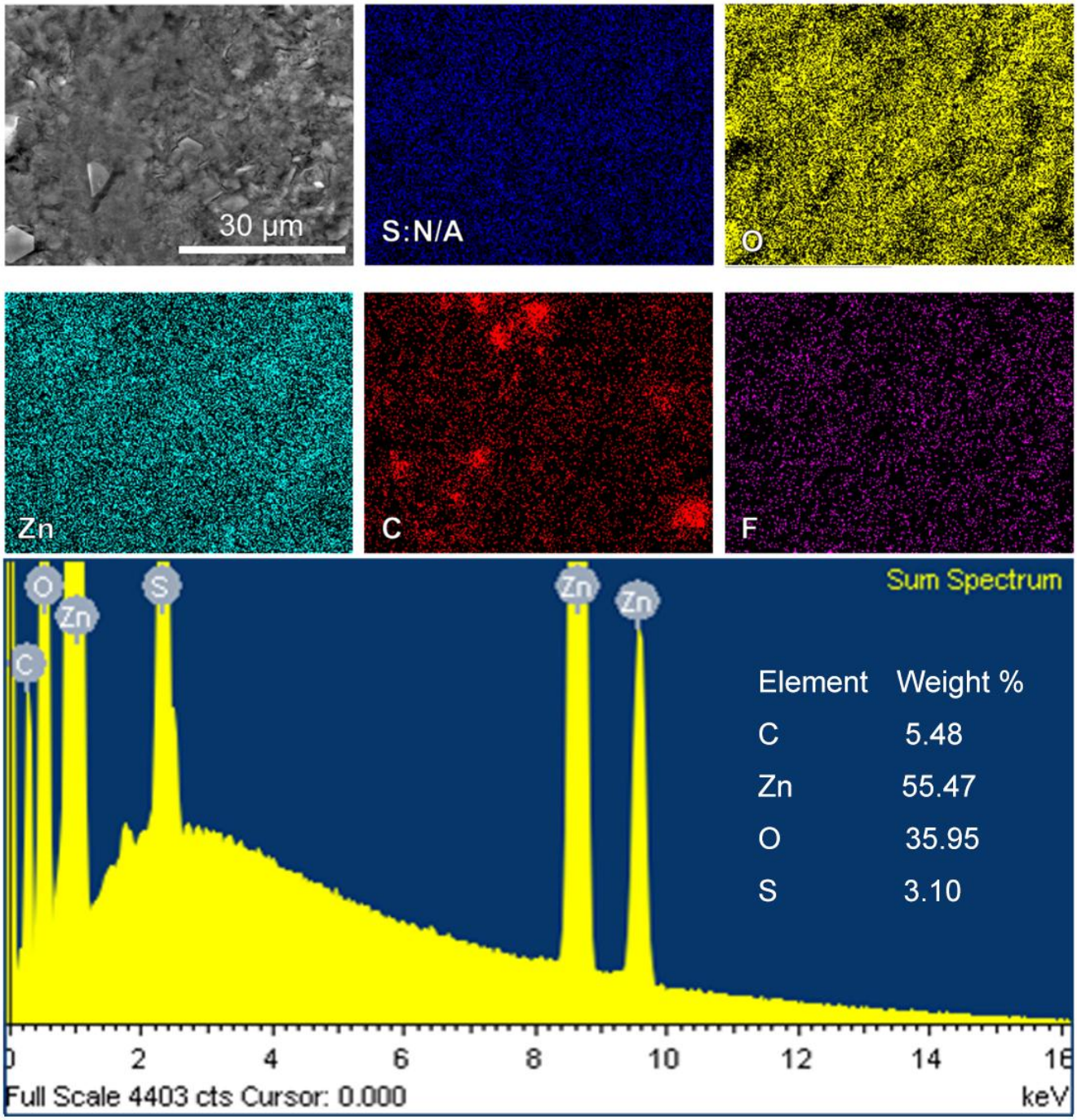

Fig. S28 The Zn anode and the corresponding EDS images soaked in the ZSF (ZSF-80) electrolyte.

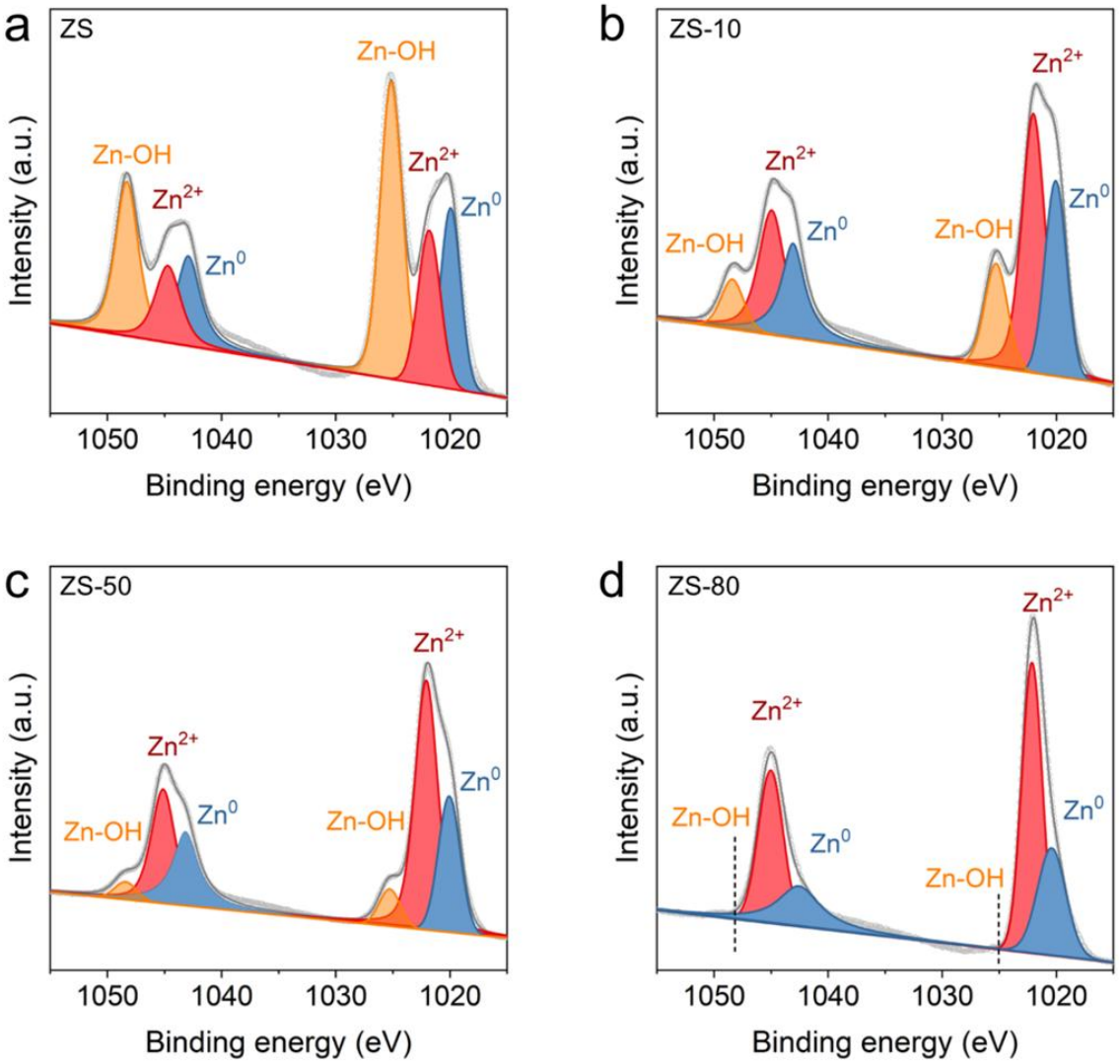

Fig. S29 (a-d) The Zn 2p XPS results of Zn foils soaked in ZS (a), ZSF-10 (b), ZSF-50 (c), and ZSF-80 (d) electrolytes.

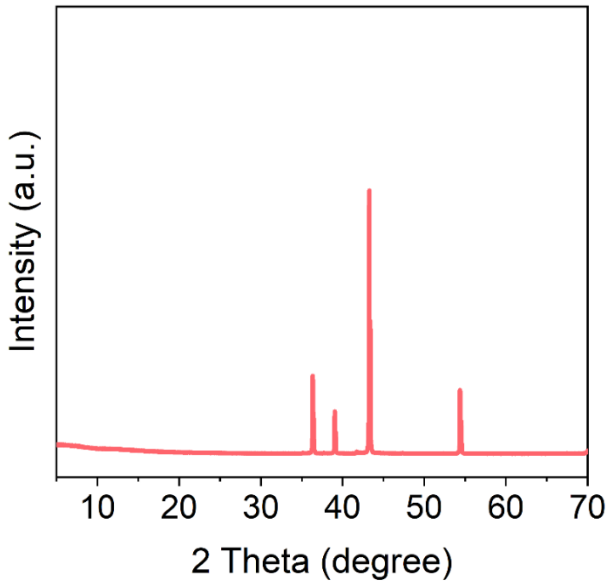

Fig. S30 The XRD pattern of the Zn soaked in ZSF electrolyte.

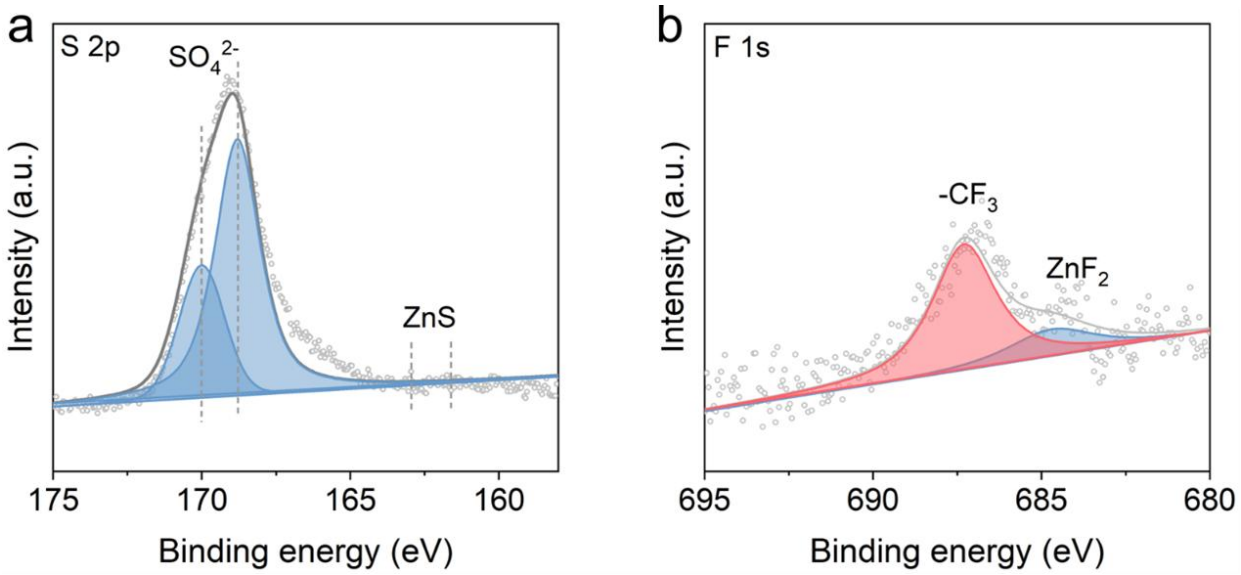

Fig. S31 The S 2p (a) and F 1s (b) XPS patterns of the Zn anode soaked in ZSF electrolyte.

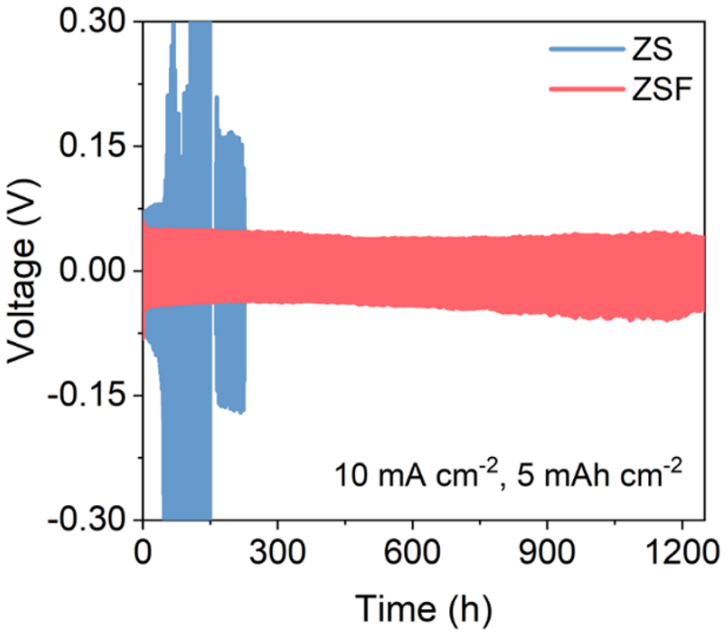

Fig. S32 Galvanostatic Zn plating/stripping in Zn||Zn symmetrical cells at current density of 10 mA cm^{-2} with a capacity of 5 mAh cm^{-2}.

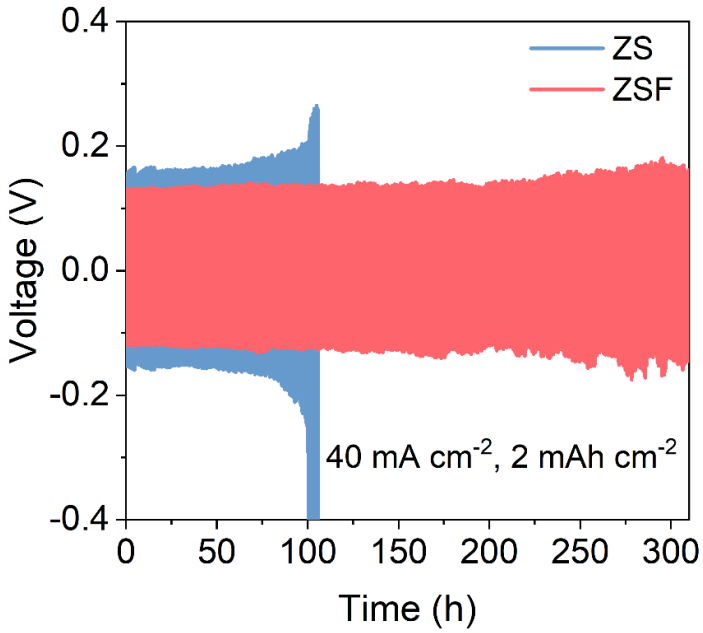

Fig. S33 Galvanostatic Zn plating/stripping in Zn||Zn symmetrical cells at current density of 40 mA cm^{-2} with a capacity of 2 mAh cm^{-2}.

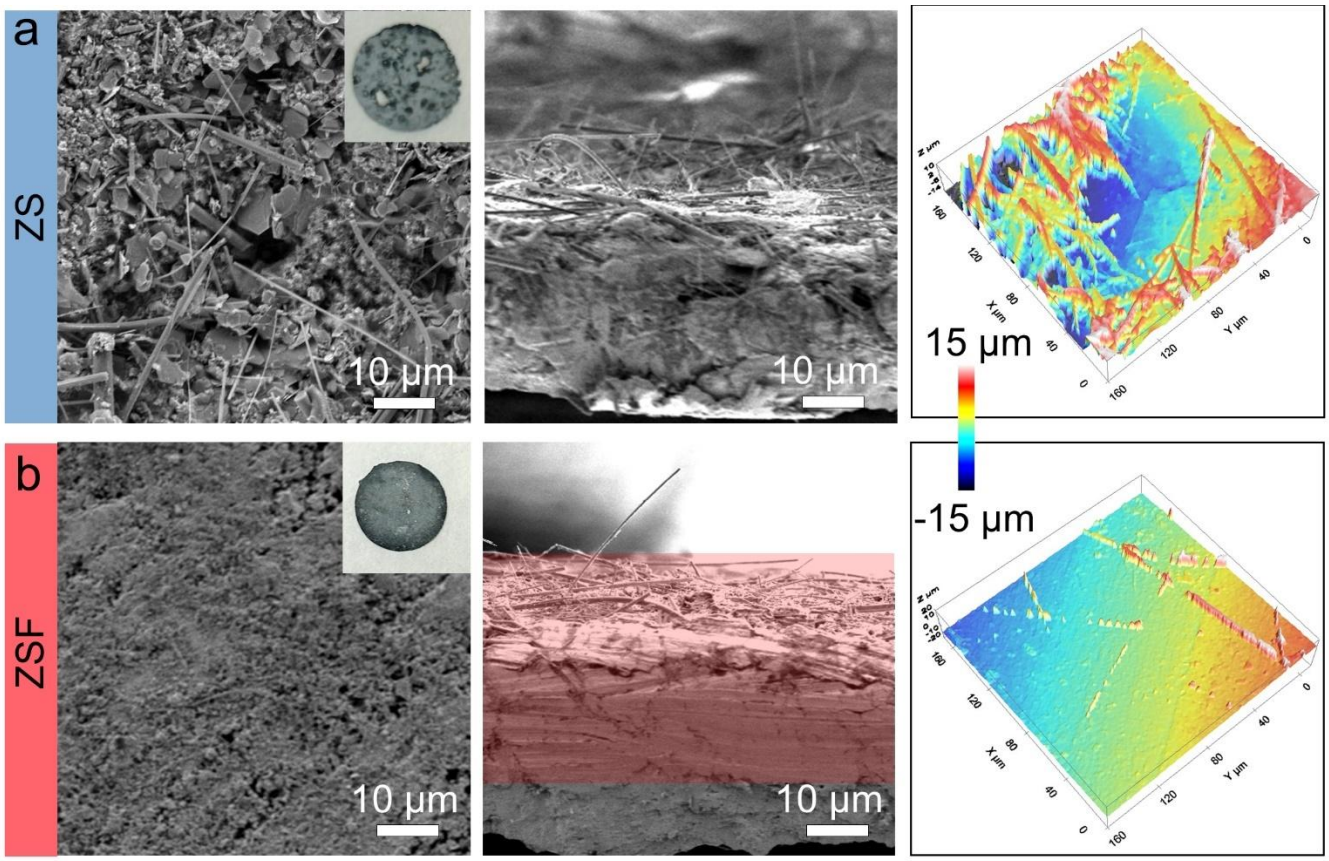

Fig. S34 Morphologies of Zn anode in ZS (a) and ZSF (b) electrolytes with a DOD of 87.1% after 100 cycles.

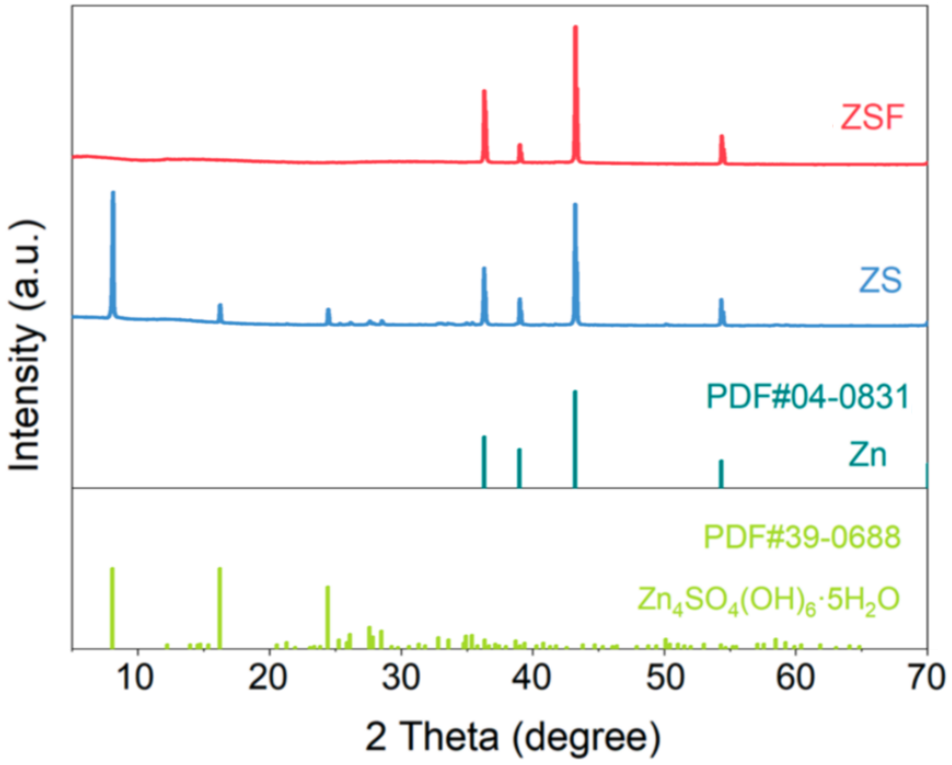

Fig. S35 The XRD pattern of the cycled Zn anode with a DOD of 87.1%.

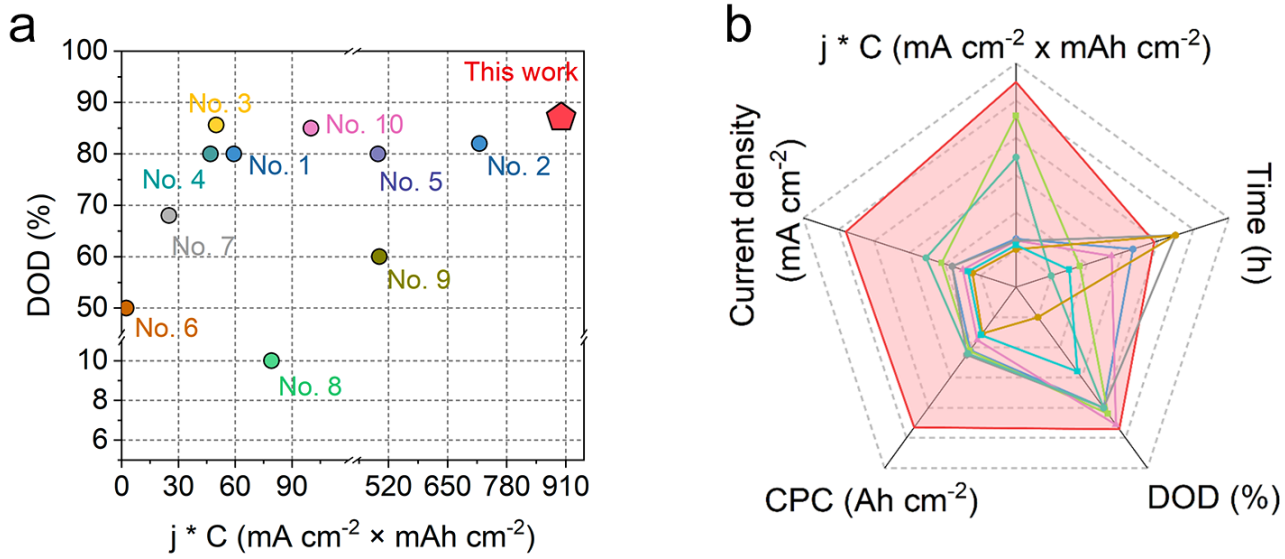

Fig. S36 (a) Comparison of DOD and j*C with previously reported results (j-current density, C-capacity).[1-10] (b) Multiple parameter comparisons with other reported Zn||Zn symmetric batteries.

Table S2 Multiple parameter comparisons with other reported Zn||Zn symmetric batteries.

Electrolyte/Anode	DOD (%)	CPC (Ah cm^{-2})	Time (h)	Current density (mA cm^{-2})	J*C (mA cm^{-2} ×mAh cm^{-2})	Ref.
La^{3+}-ZS	80	0.79	160	10	59.3	[1]
Zn@ZnP	82	0.825	110	15	720	[2]
ZnF_2-Ag@Zn	85.6	0.35	140	5	50	[3]
AZO@Zn	80	1	200	10	46.9	[4]
Zn@ZCO	80	0.093504	83	22.29	496.8441	[5]
4 m $Zn(BF_4)_2$/EG	50	0.05	200	0.5	2.5	[6]
50%PC-sat	68	0.125	100	2.5	25	[7]
2+0.1 LB	75	1.17	78	30	1050	[11]
$Zn(CF_3COO)_2$	51.24	~0.225	~75	5	18	[12]
$ZnSO_4$-H_2O-NMP	85.6	0.5	200	5	50	[13]
BE + 6M	85.3	0.2	400	1	25	[14]
HD-OTf/Li	65	1.5	1500	2	12.6	[15]
TMB-5	57	0.875	350	5	50	[16]
ZSF	87.1	5.4	180	60	900	This work

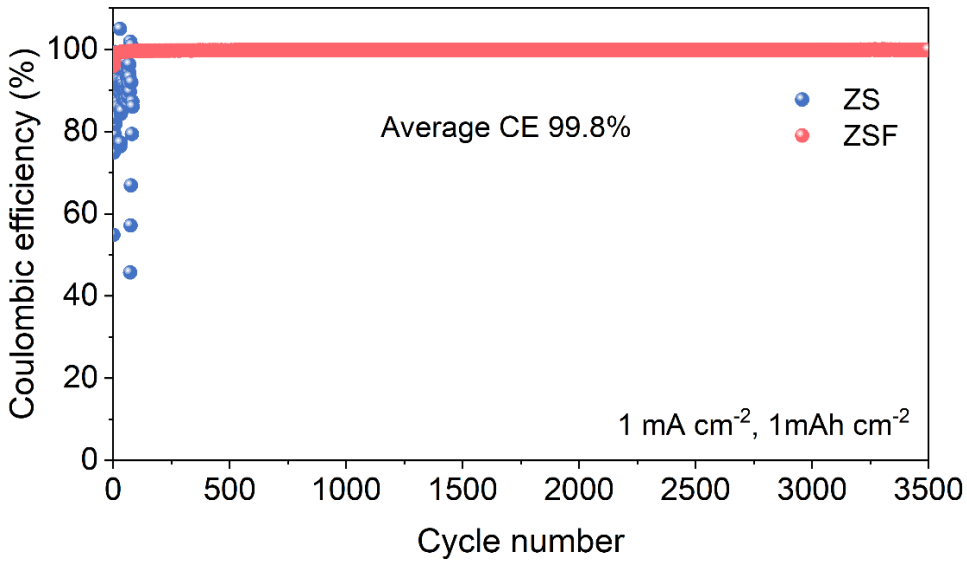

Fig. S37 The CE of Zn||Cu half cells at 1 mA cm^{-2} with a capacity of 1 mAh cm^{-2}.

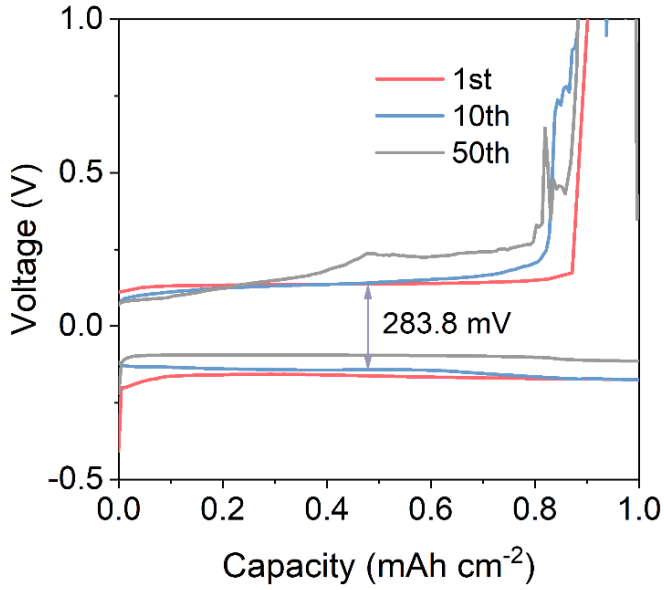

Fig. S38 Voltage profiles at various cycles in ZS electrolyte (10 mA cm^{-2}, 1 mAh cm^{-2}).

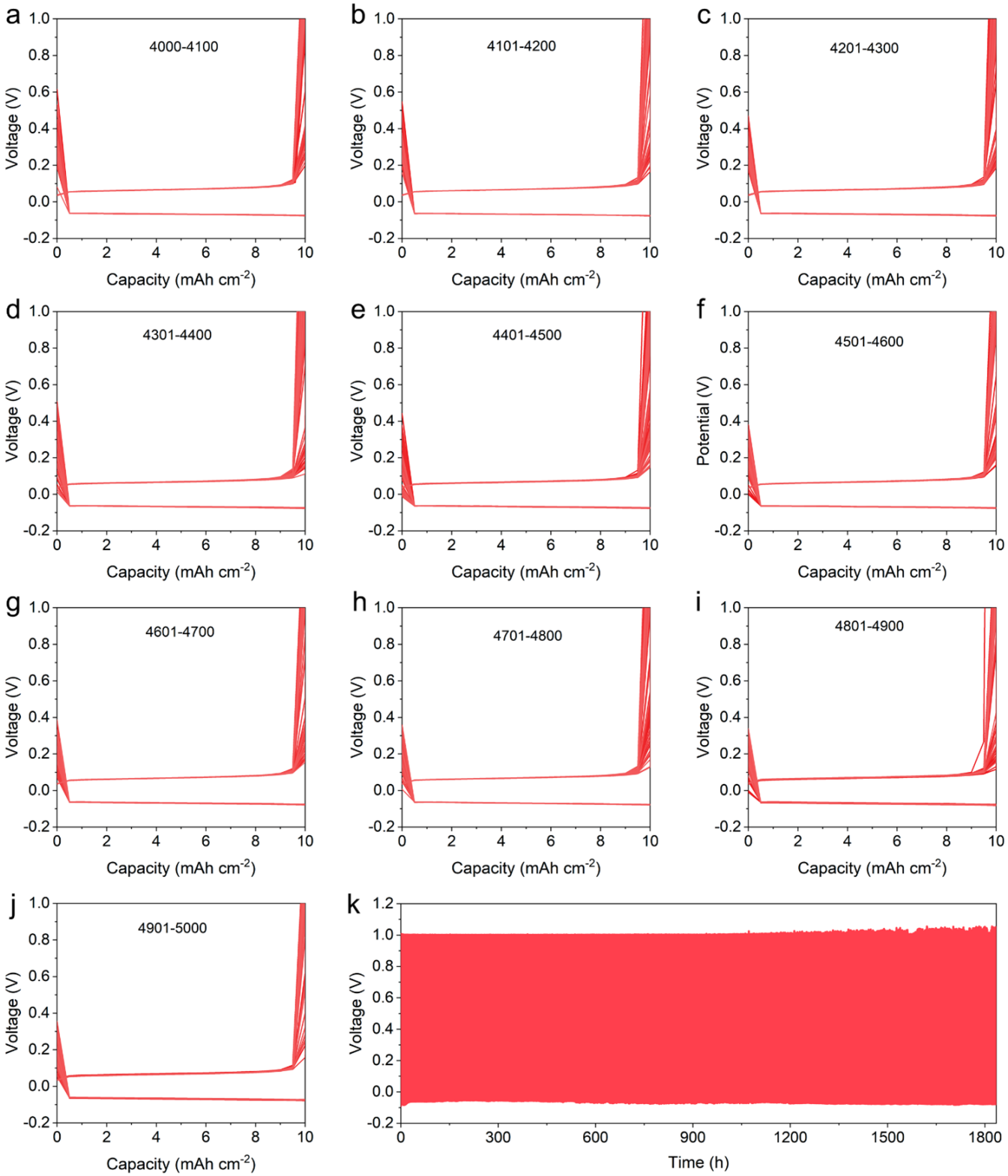

Fig. S39 (a-j) The capacity-voltage curve of 4000-5000 cycles in ZSF electrolyte (60 mA cm^{-2}, 15 mAh cm^{-2}). (k) The time-voltage curve in ZSF electrolyte (60 mA cm^{-2}, 15 mAh cm^{-2})

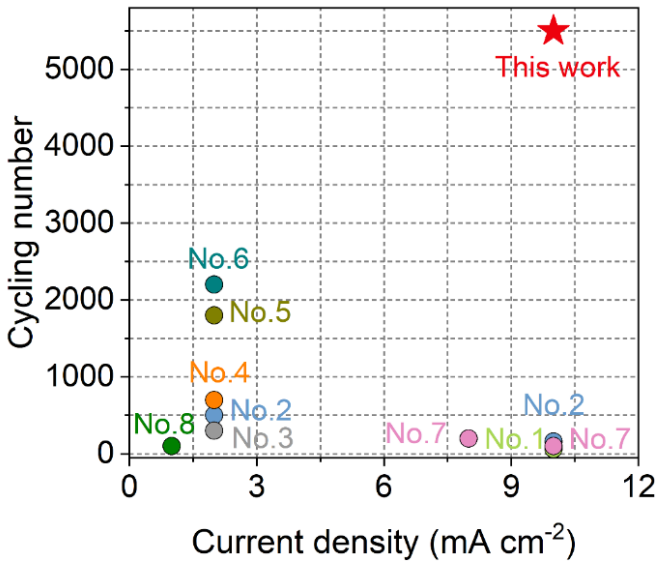

Fig. S40 The comparison of CE with other reported literatures.[1, 17-23]

Table S3 The CE with other reported Zn||Cu or Zn||Ti batteries.

Electrolyte/Anode	CE (%)	Current density (mA cm^{-2})	Cycling number	Ref.
ZSO/Ce	99.7	10	60	[17]
1 M $ZnSO_4$ + 2 wt% PDD	99.8	2	500	[18]
1 M $ZnSO_4$ + 2 wt%	99.1	10	150	[18]
10% TG	99.7	0.5	1000	[19]
10% TG	99.49	2	300	[19]
Gly/$ZnSO_4$	99.68	2	650	[20]
2 M $ZnSO_4$ + 0.1 MSG	99.75	2	1700	[21]
La^{3+}-ZS	99.9	2	2100	[1]
$Zn(OTF)_2$-HMPA-H_2O	99.5	8	200	[22]
$Zn(OTF)_2$-HMPA-H_2O	99.4	10	100	[22]
LIAE-20%	99.74	1	100	[23]
ZSF	99.7	10	6000	This work

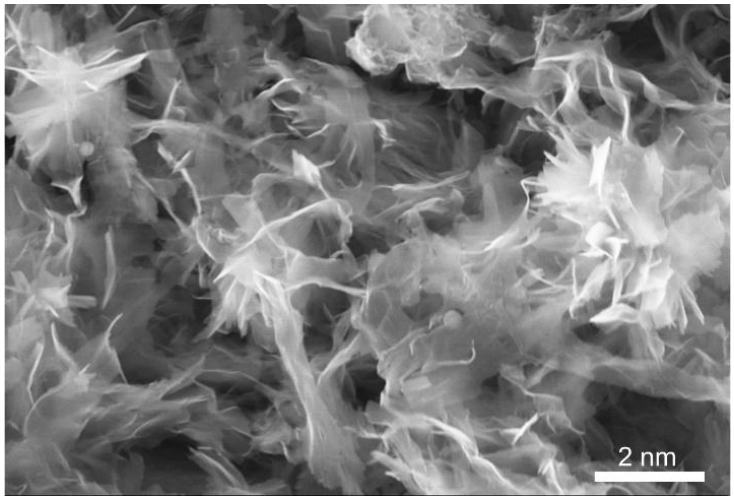

Fig. S41 SEM image of the V_2O_5 cathode material for the full-battery cell.

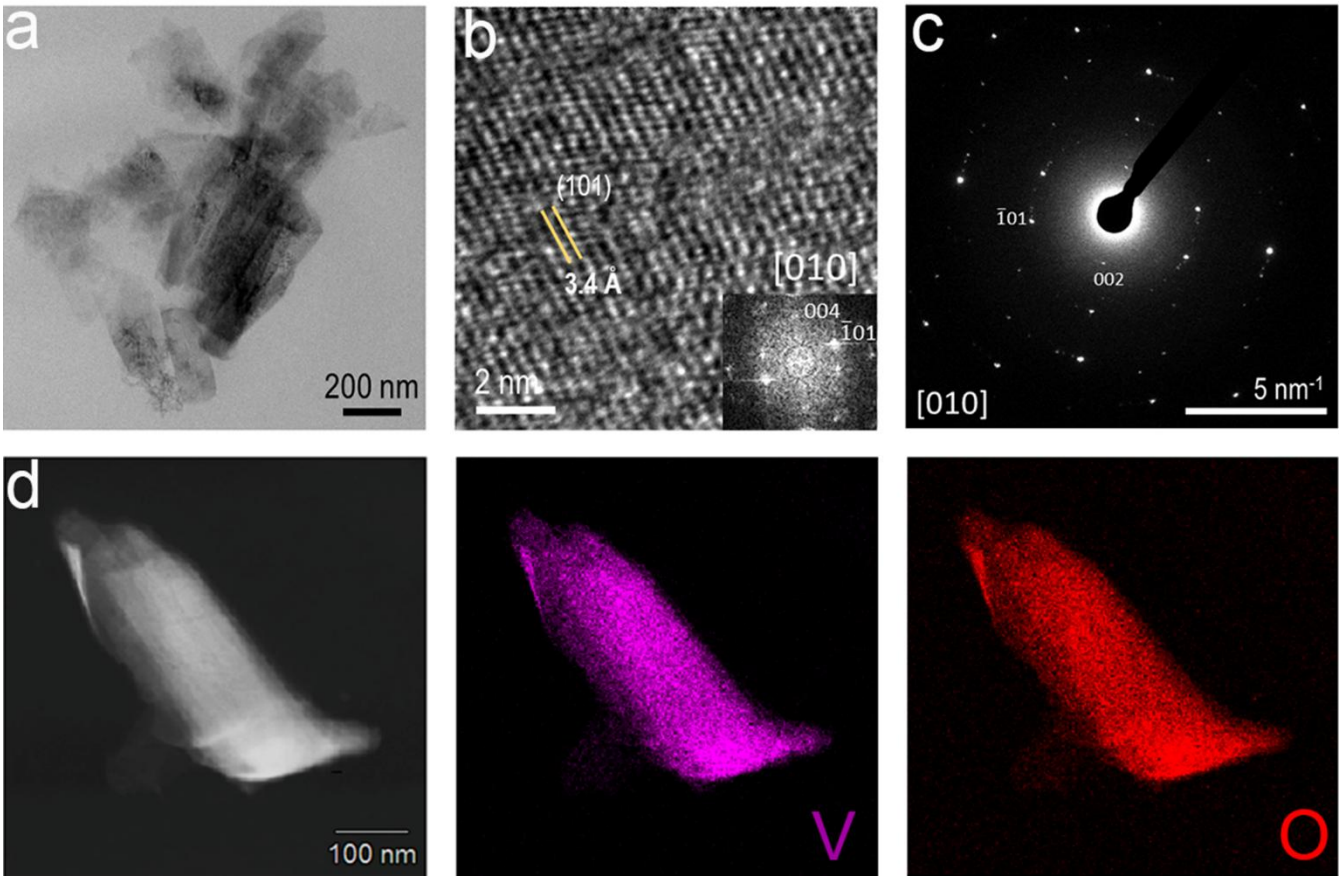

Fig. S42 (a-d) TEM (a), HRTEM (b), SAED (c), and element mappings (d) of the prepared V_2O_5 material.

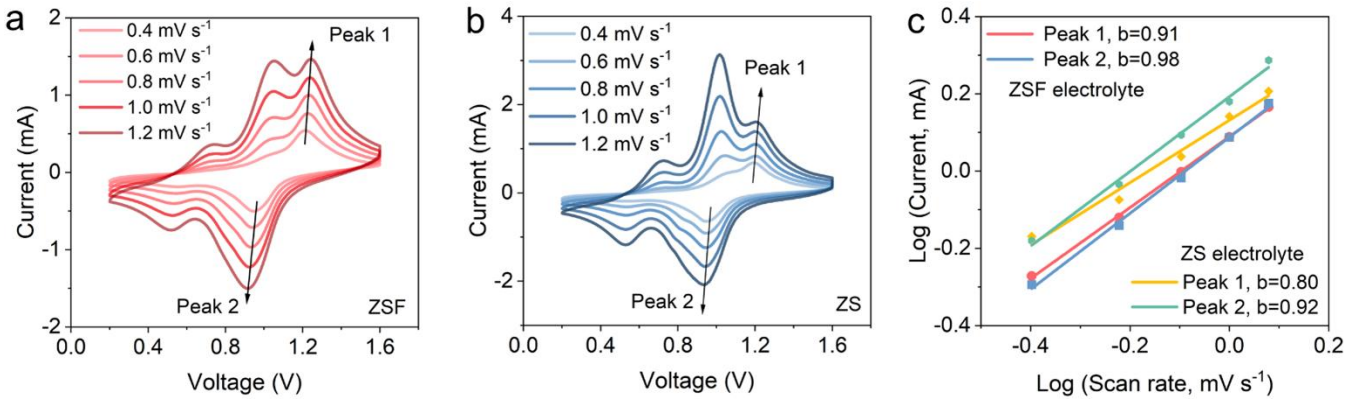

Fig. S43 The CV curve using ZSF electrolyte (a) and ZS electrolyte (b). (c) Linear fit of peak current versus square root of scan rate.

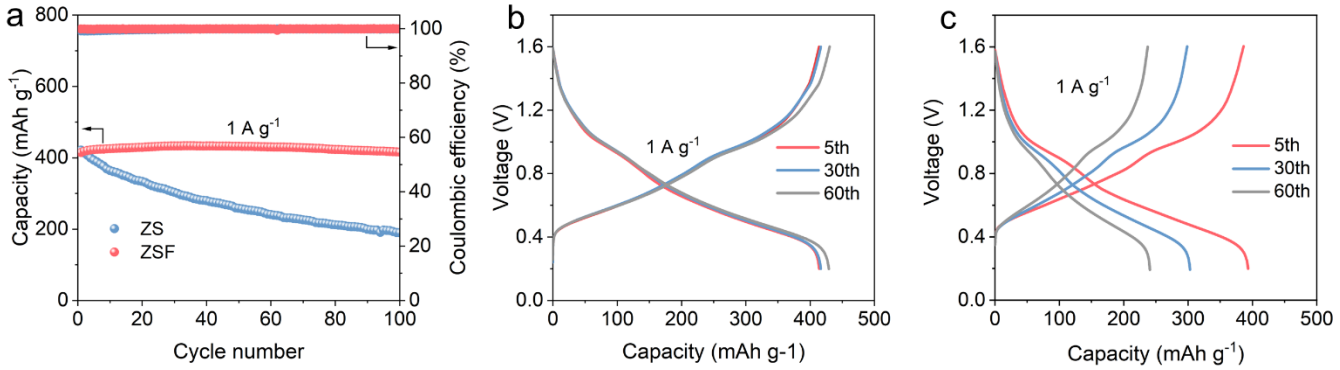

Fig. S44 Electrochemical performance of Zn||V_2O_5 full-battery cells. (a) Cycling stability at 1 A g^{-1}. Capacity-voltage curves with the ZSF (b) and ZS (c) electrolyte.

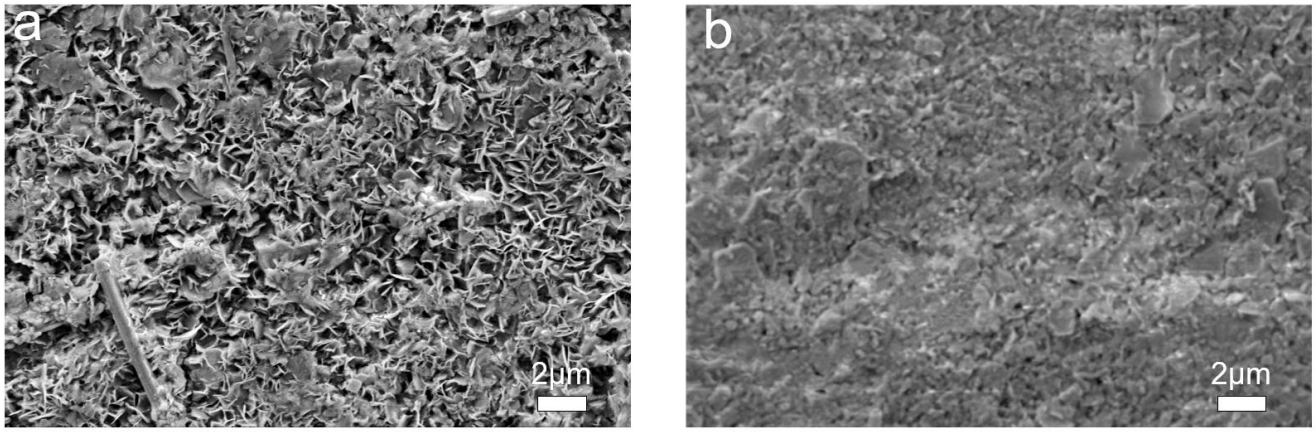

Fig. S45 (a, b) The SEM images of the Zn anodes disassembled from Zn||V_2O_5 full-battery cells after 1000 cycles in ZS (a) and ZSF (b) electrolytes.

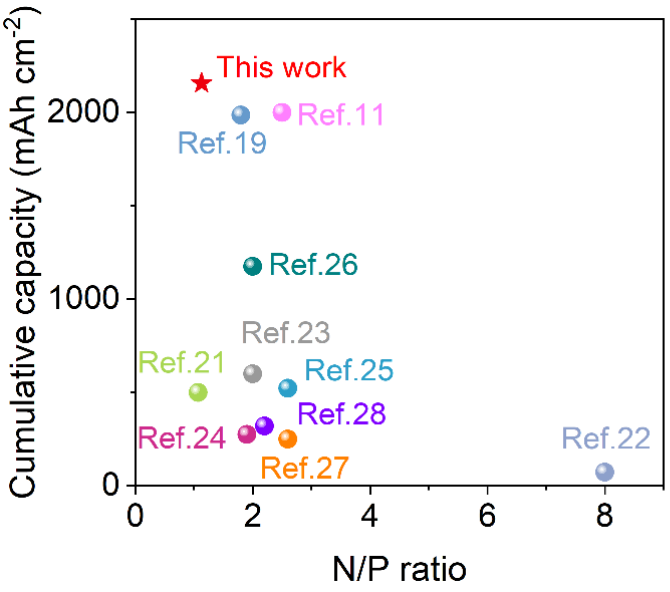

Fig. S46 Comparison of the cycling performance of Zn||V_2O_5 full-battery cells.

Fig. S47 Four series-connected pouch-battery cells powering a light board.

Table 4 The capacity comparison with other reported full-battery cells.

System	Electrolyte/Anode	N/P ratio	Cumulative Capacity (mAh cm^{-2})	Ref.
Zn||V_2O_5	Zn(OTF)$_2$-HMPA-H_2O	1.8	1986	[22]
Zn||V_6O_{13}	1Z-5H	1.07	~500	[24]
Zn||MnO_2	Sel/$ZnSO_4$	8	~72.6	[25]
Zn||MnO_2	GSS 2:1	2	~600	[26]
Zn||V_6O_{13}·H_2O	With ET	1.9	~275	[8]
Zn||I	Be-Ace-I	2.5	~2000	[14]
Zn||MnO_2	TPPS/$ZnSO_4$	2.6	~522	[27]
Zn||VO_2	M56	2	1175	[28]
Zn||VO_2	$ZnSO_4$+DGME	2.6	~250	[29]
Zn||$Zn_{0.25}V_2O_5$·nH_2O	12-C-4	2.2	~320	[30]
Zn||V_2O_5	ZSF	1.13	2156	This work

REFERENCES

1. R. Zhao, H. Wang, H. Du, Y. Yang, Z. Gao, L. Qie and Y. Huang, *Nat Commun*, 2022, **13**, 3252.
2. P. Cao, X. Zhou, A. Wei, Q. Meng, H. Ye, W. Liu, J. Tang and J. Yang, *Advanced Functional Materials*, 2021, **31**, 2100398.
3. D. Wang, D. Lv, H. Peng, N. Wang, H. Liu, J. Yang and Y. Qian, *Nano Letters*, 2022, **22**, 1750-1758.
4. H. Jin, S. Dai, K. Xie, Y. Luo, K. Liu, Z. Zhu, L. Huang, L. Huang and J. Zhou, *Small*, 2022, **18**, 2106441.
5. P. Wang, S. Liang, C. Chen, X. Xie, J. Chen, Z. Liu, Y. Tang, B. Lu and J. Zhou, *Advanced Materials*, 2022, **34**, 2202733.
6. D. Han, C. Cui, K. Zhang, Z. Wang, J. Gao, Y. Guo, Z. Zhang, S. Wu, L. Yin, Z. Weng, F. Kang and Q.-H. Yang, *Nature Sustainability*, 2021, **5**, 205-213.
7. F. Ming, Y. Zhu, G. Huang, A. H. Emwas, H. Liang, Y. Cui and H. N. Alshareef, *J Am Chem Soc*, 2022, **144**, 7160-7170.
8. K. Wang, T. Qiu, L. Lin, H. Zhan, X.-X. Liu and X. Sun, *ACS Energy Letters*, 2024, **9**, 1000-1007.
9. D. Wang, H. Liu, D. Lv, C. Wang, J. Yang and Y. Qian, *Advanced Materials*, 2023, **35**, 2207908.
10. Z. Zhao, J. Zhao, Z. Hu, J. Li, J. Li, Y. Zhang, C. Wang and G. Cui, *Energy & Environmental Science*, 2019, **12**, 1938-1949.
11. Z. Zhang, Y. Zhang, M. Ye, Z. Wen, Y. Tang, X. Liu and C. C. Li, *Angewandte Chemie International Edition*, 2023, **62**, e202311032.
12. M. Wu, X. Wang, F. Zhang, Q. Xiang, Y. Li and J. Guo, *Energy & Environmental Science*, 2024, **17**, 619-629.
13. D. Wang, D. Lv, H. Liu, S. Zhang, C. Wang, C. Wang, J. Yang and Y. Qian, *Angewandte Chemie International Edition*, 2022, **61**, e202212839.
14. K. Qiu, G. Ma, Y. Wang, M. Liu, M. Zhang, X. Li, X. Qu, W. Yuan, X. Nie and N. Zhang, *Advanced Functional Materials*, 2024, **34**, 2313358.
15. X. Zhang, Z. Deng, C. Xu, Y. Deng, Y. Jia, H. Luo, H. Wu, W. Cai and Y. Zhang, *Advanced Energy Materials*, 2023, **13**, 2302749.
16. Z. Zha, T. Sun, D. Li, T. Ma, W. Zhang and Z. Tao, *Energy Storage Materials*, 2024, **64**, 103059.
17. Z. Hu, F. Zhang, Y. Zhao, H. Wang, Y. Huang, F. Wu, R. Chen and L. Li, *Advanced Materials*, 2022, **34**, e2203104.
18. M. Peng, X. Tang, K. Xiao, T. Hu, K. Yuan and Y. Chen, *Angewandte Chemie International Edition*, 2023, **62**, e202302701.
19. Z. Liu, R. Wang, Q. Ma, J. Wan, S. Zhang, L. Zhang, H. Li, Q. Luo, J. Wu, T. Zhou, J. Mao, L. Zhang, C. Zhang and Z. Guo, *Advanced Functional Materials*, 2023, **33**, 2214538.
20. Y. Liu, Y. An, L. Wu, J. Sun, F. Xiong, H. Tang, S. Chen, Y. Guo, L. Zhang, Q. An and L. Mai, *ACS Nano*, 2023, **17**, 552-560.
21. Y. Zhong, Z. Cheng, H. Zhang, J. Li, D. Liu, Y. Liao, J. Meng, Y. Shen and Y. Huang, *Nano Energy*, 2022, **98**, 107220.
22. D. Wang, D. Lv, H. Peng, C. Wang, H. Liu, J. Yang and Y. Qian, *Angewandte Chemie International Edition*, 2023, **62**, e202310290.
23. R. Wang, M. Yao, M. Yang, J. Zhu, J. Chen and Z. Niu, *Proc Natl Acad Sci U S A*, 2023, **120**, e2221980120.
24. M. Kim, J. Lee, Y. Kim, Y. Park, H. Kim and J. W. Choi, *Journal of the American Chemical Society*, 2023, **145**, 15776-15787.
25. C. Huang, X. Zhao, Y. Hao, Y. Yang, Y. Qian, G. Chang, Y. Zhang, Q. Tang, A. Hu and X. Chen, *Advanced Functional Materials*, 2022, **32**, 2112091.
26. J. Zheng, Q. Zhao, T. Tang, J. Yin, C. D. Quilty, G. D. Renderos, X. Liu, Y. Deng, L. Wang, D. C. Bock, C. Jaye, D. Zhang, E. S. Takeuchi, K. J. Takeuchi, A. C. Marschilok and L. A. Archer, *Science*, 2019, **366**, 645-648.
27. X. Zhao, Y. Wang, C. Huang, Y. Gao, M. Huang, Y. Ding, X. Wang, Z. Si, D. Zhou and F. Kang, *Angewandte Chemie International Edition*, 2023, **62**, e202312193.
28. W. Xu, J. Li, X. Liao, L. Zhang, X. Zhang, C. Liu, K. Amine, K. Zhao and J. Lu, *Journal of the American Chemical Society*, 2023, **145**, 22456-22465.
29. B. Xie, Q. Hu, X. Liao, X. Zhang, H. Lang, R. Zhao, Q. Zheng, Y. Huo, J. Zhao, D. Lin and X.-L. Wu, *Advanced Functional Materials*, 2023, **33**, 2311961.
30. Y. Wang, B. Liang, J. Zhu, G. Li, Q. Li, R. Ye, J. Fan and C. Zhi, *Angewandte Chemie International Edition*, 2023, **62**, e202302583.